Design and Fabrication of Perovskite Micro-Cavity Lasers

Conner K. Ballew

A thesis

submitted in partial fulfillment of the

requirements for the degree of

Master of Science in Electrical Engineering

University of Washington

2016

Committee:

Lih Y. Lin, Chair

Arka Majumdar

Program Authorized to Offer Degree:

Electrical Engineering

University of Washington

Abstract

Design and Fabrication of Perovskite Micro-Cavity Lasers

Conner K. Ballew

Chair of the Supervisory Committee:
Professor Lih Y. Lin
Electrical Engineering

Over the past several years, research of methylammonium trihalide perovskite solar cells has led to a rapid increase in the efficiency of single p-n junction perovskite solar cells, from 6.5% in 2012 to 22.1% in 2016. Favorable optical properties make $CH_3NH_3PbI_3$ perovskite a promising candidate for performing at the Shockley-Queisser limit; the theoretical maximum efficiency of single p-n junction solar cells, and a commonly cited goal for photovoltaics researchers. To operate at this limit, the gain material must exhibit purely radiative recombination. Thus, research in photovoltaics is actively trying to improve the quality of thin-film perovskite in order to maximize its efficiency not only as a light absorber, but as a light emitting material.

A high-quality optical micro-cavity requires patterning of microstructures, which is made difficult by perovskite's sensitivity to chemicals used in conventional fabrication processes. This thesis describes three designs of a perovskite laser: 1) a silicon nitride photonic crystal cavity coupled to a perovskite gain medium, 2) whispering-gallery mode lasers made by chemically reflowing perovskite, and 3) an electrically-pumped distributed feedback laser.

TABLE OF CONTENTS

ACKNOWLEDGEMENTS

Thank you Laurence and Lucille Fray, whose financial support through the Fray Scholarship helped fund my education.

Chapter 1. Introduction

Perovskite has become a popular material in solar cells over the past five years. Its rapid growth in efficiency is pushing perovskite solar cells to the theoretical Shockley-Queisser (SQ) limit, which is the maximum possible efficiency of a basic, single p-n junction solar cell [1]. To operate at the SQ limit the gain material must exhibit purely radiative recombination. This necessity has pushed photovoltaics researchers to improve the quality of perovskite as both a light absorbing and light emitting material.

Perovskite refers to a general crystal structure of the form ABX_3, where A and B are cations that are both joined to an anion X. The most explored perovskites are the Methylammonium (MA) lead trihalide perovskites of the form $CH_3NH_3PbX_nY_{3-n}$, where X and Y can be I, Br, or Cl anions. These perovskites are a promising candidate for reaching the SQ limit because of their extraordinary photonic properties. They feature a tunable bandgap based on chemical composition, which is a desirable property since the SQ limit is bandgap dependent. $CH_3NH_3PbI_3$ has a bandgap of ~1.4 eV, which is conveniently near the optimal bandgap of 1.34 eV according to the SQ limit. $CH_3NH_3PbI_3$ has been the most studied perovskite structure, and is the only perovskite discussed in this thesis. It can be assumed that any use of the term perovskite refers to $CH_3NH_3PbI_3$, unless otherwise noted.

Perovskite also features a direct bandgap, which favors radiative recombination over non-radiative. The rate of non-radiative Auger recombination, even at high injection currents, has been shown to be remarkably low among solution-cast semiconductor [2]. Improvement of thin-film deposition techniques continues to improve the quality of perovskite films, reducing the number of charge-trapping defects that contribute to non-radiative recombination, and the

research of post-deposition treatments of thins films to cure pin-holes and other large defects is an area of active research [3], [4].

A large band edge absorption implies that perovskite can efficiently convert light into electric current, which indicates its ability to provide high optical gain when used as a laser gain medium [2]. Furthermore, perovskite features a small Stokes shift [5]. This small Stokes shift allows for efficient pumping of the gain material, since less energy is dissipated as heat when excitons relax to the band edge.

Perovskite has already shown to be a capable light emitting material [6]–[15]. However, due to perovskite's rapid degradation in polar solvents and ambient moisture, the fabrication of a high-quality perovskite micro-cavities remains challenging. Some of the currently reported perovskite lasing structures are created from naturally formed polygonal crystal grains, but these grains have random positions and sizes which hurts the controllability of these devices [15]. Other lasing structures have been demonstrated using artificially patterned cavities, such as a glass photonic crystal (PhC) with spin-cast perovskite filling in the glass features [6]. In 2015, a distributed feedback (DFB) structure was formed by evaporating perovskite onto a patterned grating [14]. It is unclear whether the device achieved lasing via optical pumping, however the demonstration of a DFB laser architecture may pave the way for an electrically-pumped perovskite laser. DFB lasers are well-suited for industrial applications, so this will most likely be an avenue of intense research.

This thesis describes three methods for creating a perovskite laser. Chapter 2 describes the relevant background for each method, and details the basic theory of lasers and various optical resonators. Chapter 3 describes the design of a silicon nitride photonic crystal cavity (PhCC) that can be coupled to a perovskite gain medium. Chapter 4 describes a method that

utilizes chemical reflow to potentially create smooth, high-quality micro-cavity structures capable of supporting whispering-gallery modes. This research direction has a promising precedent -- reflow of silica has been used in a similar manner to make the highest quality optical resonators. By creating a silica disc and illuminating its edges with a CO_2 laser, the edges are thermally reflowed into a smooth optical resonator capable of achieving Q-factors on the order of 10^{10} [16]. Chapter 5 details the design and simulation of an electrically-pumped DFB laser, which could be the first solution-processed electrically-pumped laser if realized. Finally, Chapter 6 concludes the thesis, and discusses some future directions that perovskite laser research can take.

Chapter 2. Background Information

2.1 Lasers

Although the term "laser" is part of English vernacular, the term originated as an acronym: "**L**ight **A**mplification by the **S**timulated **E**mission of **R**adiation." The first laser was created in 1960 by Theodore Maiman, and has since grown into a multi-billion dollar industry [17].

A laser requires three components:

1. *Gain medium:* A material that emits light when excited by some external source of energy.
2. *Excitation "pump":* Any method used to excite the gain medium. This commonly includes optical pumping via an external light source, electrical pumping, or pumping via a chemical reaction.
3. *Optical resonator:* A cavity that can capture the light emitted from the gain medium. This component is required to provide positive feedback to the gain medium.

This section is devoted to analyzing how these three components work together to form a laser.

The gain medium is made of a material that radiates light when excited by an external source. This process is known as *fluorescence*. Atoms and molecules (I will only refer to atoms and their electrons from now on, for simplicity) have discrete, quantum mechanical energy levels. If there is no external source of excitation, then the population of these various energy levels are governed by the Boltzmann distribution:

$$\frac{N_2}{N_1} = exp\left(-\frac{E_2-E_1}{k_B T}\right) \tag{2.1}$$

N_2 is the number of atoms in the excited state, while N_1 is the number of atoms in the lower energy state known as the *ground state*. The difference in E_2 and E_1 represents the energy difference between these two states, and can be thought of as the amount of energy an electron must absorb from the incident photon in order for its atom to transition to the higher energy state. k_B is the Boltzmann constant, and T is the temperature of the material. Equation 2.1 shows that the population of the ground state is always greater than that of higher energy states when the material system is under no form of external excitation.

When a source of external energy is present, a material's atoms can shift to higher energy states. After a certain characteristic time known as the *relaxation time*, the excited atom will transition back to the ground state. To conserve energy this process must reemit a photon that has an energy equal to the amount of energy the recently relaxed atom lost. This process is known as *spontaneous emission*. Spontaneous emission is a stochastic process; the exact time it takes for an excited electron to relax is impossible to predict, but a large enough set of samples will yield an average relaxation time. Photons emitted by spontaneous emission have a random direction and phase, but a well-defined frequency given by Planck's Law:

$$\omega_{21} = \frac{E_2 - E_1}{\hbar} \tag{2.2}$$

ω_{21} is the frequency in radians per second of the spontaneously emitted photon, and $\hbar$ is the reduced Planck constant. A material can have many different energy levels, and thus photons of many different frequencies may be spontaneously emitted depending on the atomic transition that spawned it.

The process in which an electron absorbs a photon and is excited to a higher energy level is known as *stimulated absorption*, or just *absorption*. A reverse process also exists known as *stimulated emission*. This latter process describes the interaction between an electron in an

excited state and an incident photon with a frequency given by Equation 2.22.1. In this case, it is possible that the incident photon will force the excited electron to relax and emit a photon that is identical to the incident photon in frequency, phase, and direction of propagation. The incident photon and excited photon are therefore coherent, which lays the foundation for stimulated emission being used as a method of optical amplification.

The spontaneous and stimulated emission of photons are examples of radiative transitions. There also exists non-radiative transitions, in which the energy that an excited atom loses during the transition is converted to heat within the material lattice. This is an undesirable property in lasing, as it hurts the efficiency of a light-emitter. However, non-radiative processes are often unavoidable consequences of a huge variety of material properties, and must be considered in any sort of accurate modeling of photonic behavior.

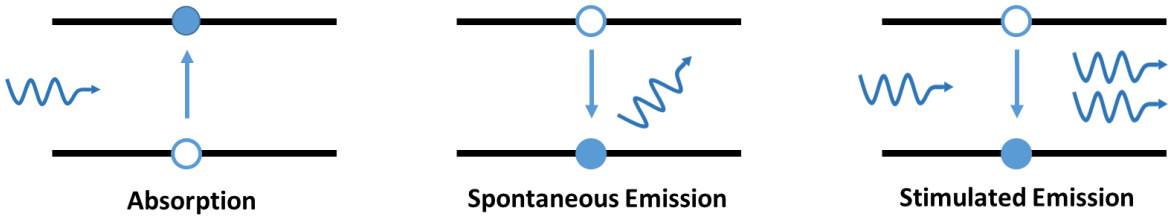

Figure 1: Photon-electron interactions in a quantum system.

The population of states in a 2-level system can be mathematically described by the *atomic rate equations*. Although I have not yet discussed how this is necessary for lasing, these equations are often referred to as the *laser rate equations* when they are used in the context of lasers. These equations balance the rates of atomic transitions within the material. The rate of decay γ_{21} from state E_2 to E_1 due to both spontaneous emission and non-radiative transitions

causes a decrease in the population of the state E_2 at a rate that is directly proportional to the population of the state E_2.

$$\frac{dN_{2,spontaneous}(t)}{dt} = -\gamma_{21}N_2(t) \tag{2.3}$$

This rate of population change is equal and opposite for the E_1 state.

$$\frac{dN_{1,spontaneous}(t)}{dt} = \gamma_{21}N_2(t) \tag{2.4}$$

The rate of stimulated emission is directly proportional to the number of incident photons, as well as the number of available electrons in the E_2 state. The rate of absorption is similarly proportional to the number of incident photons, but is proportional to the E_1 population instead of E_2.

$$\frac{dN_{2,stimulated}(t)}{dt} = -Kn(t)N_2(t) \tag{2.5}$$

$$\frac{dN_{2,absorption}(t)}{dt} = Kn(t)N_1(t) \tag{2.6}$$

Here, n(t) denotes a time dependent incident photon number, and K is a constant of proportionality. n(t) itself is directly proportional to the excitation light intensity. These rate equations can be summed to solve for the total rate of change of both state populations

$$\frac{dN_2(t)}{dt} = -\frac{dN_1(t)}{dt} = Kn(t)[N_1(t) - N_2(t)] - \gamma_{21}N_2(t) \tag{2.7}$$

Every transition from E_2 to E_1 that is due to stimulated emission will add a quantum of energy *hv* to the input signal defined by n(t), and every absorption will subtract *hv* from the input signal. This can be written as:

$$\frac{dU(t)}{dt} = K[N_2(t) - N_1(t)] * n(t)h\nu \tag{2.8}$$

U(t) is the energy density of the input excitation light. The term *n(t)hv* is simply the signal energy density U(t), so this expression can be rewritten entirely in terms of either energy density U(t) or signal photon count n(t). The latter is expressed as:

$$\frac{dn(t)}{dt} = K[N_2(t) - N_1(t)] * n(t) \tag{2.9}$$

Equation 2.9 is expressed in such a way that directly implies the mechanism for light amplification. If the population of state E_2 is larger than the population of state E_1, then the rate of change of an incident light field is increasing. This is due to stimulated emission dominating over absorption, which favors the creation of coherent light. Thus, in order for light amplification to occur the system must have an *inverted population*, meaning the higher energy states must be brought to have a higher population than the lower energy state. Since it is statistically favorable for lower energy states to be more populated in the absence of external excitation, the gain medium must be actively pumped to create an inverted population.

While the derivation of the time characteristics of a 2-level system is useful for seeing the principle of light amplification that is at the heart of laser operation, it is impossible to maintain an inverted population (and therefore amplification) in a steady-state two-level model. This can be seen from setting the time-derivatives of the state populations in equation 2.7 to zero. Solving for N_2 gives:

$$N_2 = \left(1 - \frac{\gamma_{21}}{\gamma_{21} + Kn(t)}\right) N_1 \tag{2.10}$$

Since γ_{21}, K, and n(t) are all positive quantities, the coefficient in this equation is less than unity.

$$\left(1 - \frac{\gamma_{21}}{\gamma_{21} + Kn(t)}\right) < 1$$

$$\rightarrow N_2 < N_1$$

The issue with this two-level system is that the excitation laser and the stimulated emission laser are of the same wavelength. Since there is only one definable energy difference in this model, the photons that cause stimulated emission are of the same frequency as the photons that are absorbed. Due to the probabilistic nature of these processes, this steady state calculation

simply means that absorption will ultimately become the dominant process in a two-level system, precluding the formation of a steady-state inversion population. Fortunately, this issue with a two-level system is purely due to the model being overly simplified. We need only refine our model to include more energy levels. The common model for this is a four-level model.

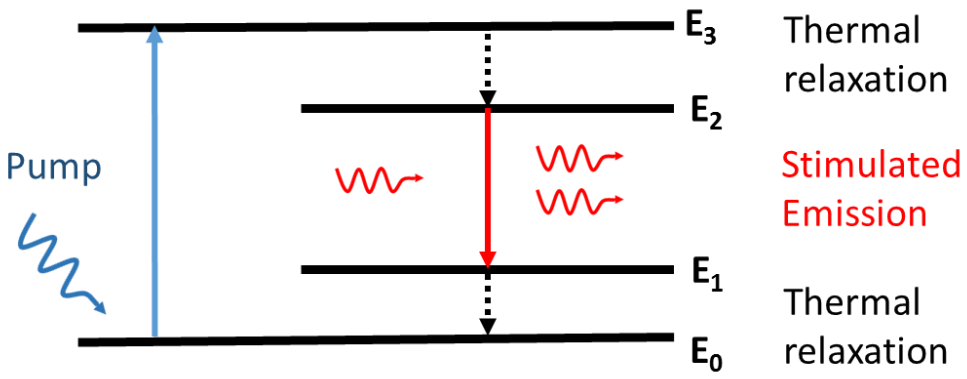

Figure 2: A four-level lasing model.

A four level model is a fairly realistic model of many materials. It consists of: a ground state E_0; two intermediate states, E_1 and E_2, such that the transition from E_2 to E_1 is radiative; and finally a high-energy state E_3. The transition from E_2 to E_1 is called the *laser transition*. By introducing new energy levels, we can now separate the pump excitation light from the light created through stimulated emission, since they will now be of different frequencies. The excitation light pumps electrons from E_0 to E_3, which must be done using a photon of comparable energy to the difference between those two levels. Excited electrons in state E_3 quickly fall down to state E_2, usually in a series of vibrational state changes that are non-radiative. E_2 must be a long-lived state relative to the other states, so that there is a sufficient amount of time for a photon to stimulate the radiative transfer from E_2 to E_1. Finally, electrons in state E_1 fall down to

E_0 and then get pumped back up to a higher energy level. It is important that the transition from E_1 to E_0 happen quickly so that laser radiation is not reabsorbed by an electron in state E_1.

The rate equations for a four-level system are derived in a similar fashion to the two-level system. However, transitions to and from every state are generally included, yielding a large amount of terms in each differential equation. Solving for the steady-state difference in the population of E_2 and E_1 gives:

$$N_2 - N_1 = \frac{R_p(\gamma_{10}-\gamma_{21})}{\gamma_{10}\gamma_{21}} = R_p\tau_{21}\left(1 - \frac{\tau_{10}}{\tau_{21}}\right) \quad (2.11)$$

R_p is the rate at which electrons relax into the state E_2. γ_{mn} is the decay rate from state *m* to state *n*, and τ_{mn} is the relaxation time for the state *m* to state *n* transition.

In this model, population inversion is achieved in the steady-state as long as the relaxation time of the upper state in the laser transition has a greater relaxation time than that of the lower state. The value of the inverted population is linearly proportional to the rate at which electrons are being pumped into the upper laser level, and is also proportional to the lifetime of this state. This suggests that a strong pump and a long-lived upper laser level state are beneficial for lasing materials.

This requirement for a strong pump and a sufficiently long-lived lifetime can be described with an analogy. Imagine you are trying to fill a bucket with sand by continuously shoveling sand into the container. If the container has a porous bottom, then the sand will leak out at some rate. The quicker the sand leaks out, the more intensely you will have to shovel sand into the container to recover what sand is lost and continue filling up the bucket. The shoveling of sand in this case is analogous to the energy that pumps the gain material, while the sand trickling through the bucket to the ground is analogous to the radiative transition of electrons falling to a lower-level state.

The working principle of optical amplification in a semiconductor is similar to that of a four-level system. In this case, electrons are excited from the valence band (VB) to the conduction band (CB). This transition can take place away from the VB maximum and the CB minimum if a pump of suitable energy is used. Following the creation of an electron in the CB and a hole in the VB, both particles will relax to their respective band's vertex. Supposing the semiconductor is a direct-bandgap material, the dominant recombination mechanism for this electron-hole pair is usually radiative. The electron-hole pair can be driven to recombine through stimulated emission, just as in the case of the four-level model. This process is depicted in Figure 3.

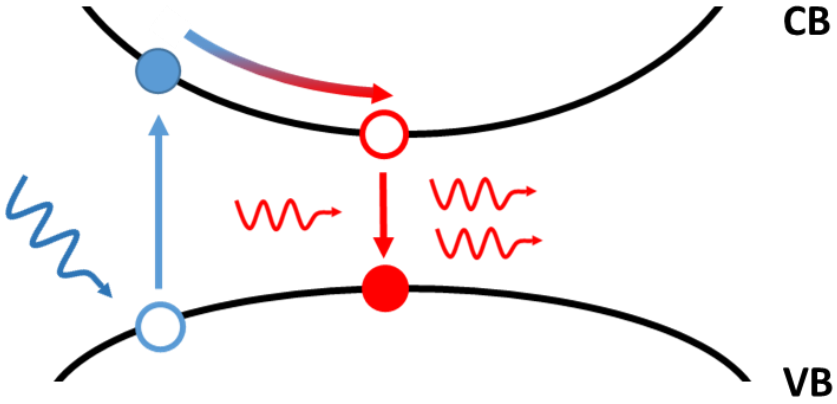

Figure 3: A semiconductor laser modeled as a four-level model.

The final requirement for a laser is an optical resonator. In the absence of a resonator, a pumped gain medium could function as an optical amplifier to an incident beam that is capable of stimulating photons. However, in order to make a self-contained laser that emits a coherent beam, there must be some mechanism of positive feedback. This is achieved with a resonator, which by some mechanism allows stimulated photons to pass through the gain medium multiple times. Furthermore, the resonator affects the output spectrum of the laser light source. For wavelengths that do not resonate, the energy will leave the cavity without having stimulated the

emission of many photons in the gain medium. For wavelengths that resonate well, photons will be repeatedly fed through the gain medium, producing more and more stimulated photons of that particular wavelength.

As an example, I will discuss a simple resonator called the *Fabry-Perot* resonator. In its most basic form it consists of two mirrors separated by a fixed distance. Resonant wavelengths are ones that constructively interfere as they propagate back and forth between the two mirrors. If light of a particular wavelength does not constructively interfere in the cavity, then the energy of this light within the cavity will rapidly decay. This resonant condition sets a requirement for the length of the cavity such that it can support a mode of light with wavelength λ.

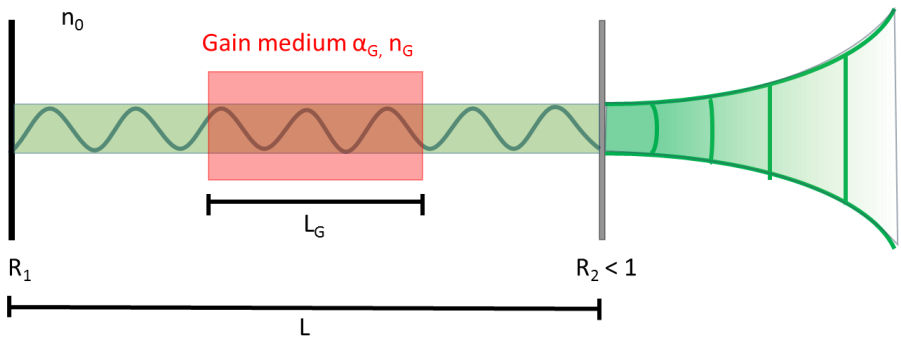

Figure 4: A Fabry-Perot lasing cavity with a gain medium.

The condition for lasing is that the round-trip gain introduced by the gain medium is greater than the losses introduced from a roundtrip through the cavity. As one ramps up the power of the pump laser, a larger population inversion can be sustained, and more optical gain is achieved. At some point, the gain will exactly counteract the losses introduced by the cavity. This point is called the *lasing threshold*. Once the pump power rises beyond the lasing threshold, some photons created through stimulated emission will survive the round-trip and will rapidly multiply in a chain-reaction like process. The growth in output power rises unhindered until the population inversion is insufficient to continue supporting the stimulation of more photons. In

other words, the gain medium cannot continue amplifying arbitrarily large input signals, so the gain decreases as the input signal increases. This is called *gain saturation*.

The cavity resonance condition and the lasing threshold for a Fabry-Perot laser can be simply calculated. Consider the laser in Figure 4. The laser consists of a laser gain medium of length L_G with a gain coefficient of α_G, embedded in a cavity of length L. For any field propagating through the gain medium, the amplitude of such a field can be described by:

$$|E| \propto \exp(\alpha_G L_G)$$

Now consider the electric field at the same spatial position in the resonator: E_i is the initial complex field, and E_f is the complex field after a single round-trip through the cavity. The relationship between these fields is given by multiplying E_i by the optical transfer function of each element.

$$\frac{E_f}{E_i} = r_1 r_2 \exp(2L_G\alpha_G)\exp(2j(L_G k_G + Lk_0 - L_G k_0)) \qquad (2.12)$$

r_1 and r_2 are the reflection coefficients of the mirrors. k_g and k_0 are the wavenumbers of the propagating wave in the gain medium and the surrounding cavity medium, respectively.
In order for resonance to occur, the phases of these fields must be equal (modulo 2π). Assuming for simplicity that the mirrors do not contribute any net phase shift (i.e. the product $r_1 r_2$ is purely real), this gives the phase condition for resonance:

$$\Delta\varphi = 2\pi m$$
$$2(L_G k_G + k_0(L - L_G)) = 2\pi m$$
$$L_G k_G + k_0(L - L_G) = \pi m \qquad (2.13)$$

m is a positive integer, indicating that the resonance condition can be satisfied by infinitely many wavelengths. In terms of a particular resonating free-space wavelength λ_0, and the refractive indices of the gain material n_G and surrounding material n_0, this can be solved for λ_0:

$$\lambda_0 = \frac{2L_G n_G + 2n_0(L - L_G)}{m} \tag{2.14}$$

The numerator of this equation is simply the round-trip optical path length of the cavity. The longitudinal modal profile of the first four solutions to this equation are shown in Figure 5. It should be noted that Fabry-Perot modes are ordinarily of a high-order for multiple reasons. First, it is difficult and expensive to fabricate Fabry-Perot cavities with lengths on the order of an optical wavelength. Furthermore, such a small cavity is often times undesireable. On the micro-scale and larger, the Q-factor scales approximately with mode volume V – that is, there exists a trade off between tight temporal confinement (Q) and small spatial confinement (V) [16].

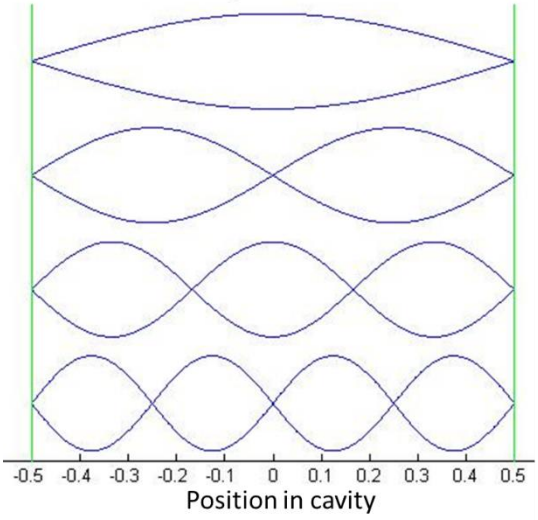

Figure 5: The first four longitudinal modes of a Fabry-Perot resonator.

The lasing threshold requires that the round-trip gain must be equal to the round-trip loss in the cavity. I will assume for simplicity that the only mechanism of loss in this system is due to the mirror reflectivites, although there can be many mechanisms for loss. These extra loss mechanisms can be accounted for by multiplying Equation 2.12 by more transfer functions that include attenuation. The amplitude condition can be written as:

$$r_1 r_2 \exp(2L_G \alpha_G) = 1$$

Squaring this equation and solving for α_G gives:

$$\alpha_G = {\ln\left(\frac{1}{R_1 R_2}\right)}\Big/{4L_G} \tag{2.15}$$

where $R_1 = |r_1|^2$, and $R_2 = |r_2|^2$. This is the gain required for lasing to occur. Although not derived here, a more common way to state this gain condition is by stating in terms of the required population inversion. When put in these terms, the amplitude condition becomes:

$$N_2 - N_1 \geq N_{th} \equiv \frac{\pi\Delta\omega}{\lambda^2\gamma_{rad}L_G} ln\left(\frac{1}{R_1 R_2}\right) \tag{2.16}$$

where N_{th} is the population inversion required for lasing, γ_{rad} is the radiative decay rate of the laser transition, and $\Delta\omega$ is the linewidth of this transition [18].

There are two observations made that indicate that a system is lasing. First, the output power versus the input pump power is measured. There are two regimes to consider: pump powers that are below the lasing threshold, and those that are above. As one increases the pump power in a system that is not lasing, there is an approximately linear rise in output power. Beyond the lasing threshold the increase in power is still linear, however the rate of increase becomes orders of magnitude larger. There is essentially no loss due to the cavity in this regime, since all loss is overcome by positive feedback which continuously regenerates the signal. Increasing the pump power leads to a larger inverted population, which allows the system to provide more gain before saturating.

The second observation is a narrowing of linewidths in the PL spectrum. This is caused by stimulated emission favoring the parts of the gain material's PL that are resonant in the cavity. As the system transitions from being governed by stimulated emission instead of spontaneous emission, the huge rise in output power occurs only at wavelengths that are resonant in the cavity.

This linewidth narrowing can also be explained as a general, mathematical consequence of a dynamical system being driven by positive feedback. The Q factor of a resonant system, such as an optical cavity, can be defined in two ways:

$$Q \equiv \frac{f_r}{f_{FWHM}} \tag{2.17}$$

$$Q \equiv 2\pi \frac{E_{stored}}{E_{lost}} \tag{2.18}$$

f_r is the resonant frequency, f_{FWHM} is the full width at half-maximum of the resonant peak, E_{stored} is the energy stored in the cavity, and E_{lost} is the energy dissipated in a single oscillation cycle. Although these different definitions yield different values for a damped cavity, they approach one another as Q gets large.

The energy definition states that the cavity Q increases if less energy is lost in a cycle. When the light emission into a cavity is due to stimulated emission, there exists a constant regenerative feedback that replaces any photon lost with a newly stimulated photon. Even though loss mechanisms in the cavity still exist, they are effectively nullified by this regenerative feedback. One can say that the *effective Q* is therefore increased when a laser is pumped beyond the threshold. According to the definition of Q given by Equation 2.17, this increase in Q also leads to a sharpening of the resonant peak, or equivalently a narrowing of the laser linewidth.

To summarize, as a light source enters the lasing regime, both an increase in output power and a sharpening of the resonant peak can be observed. An example plot of this is shown in Figure 6. These two observations of lasing are practically required to demonstrate that a light source truly is lasing.

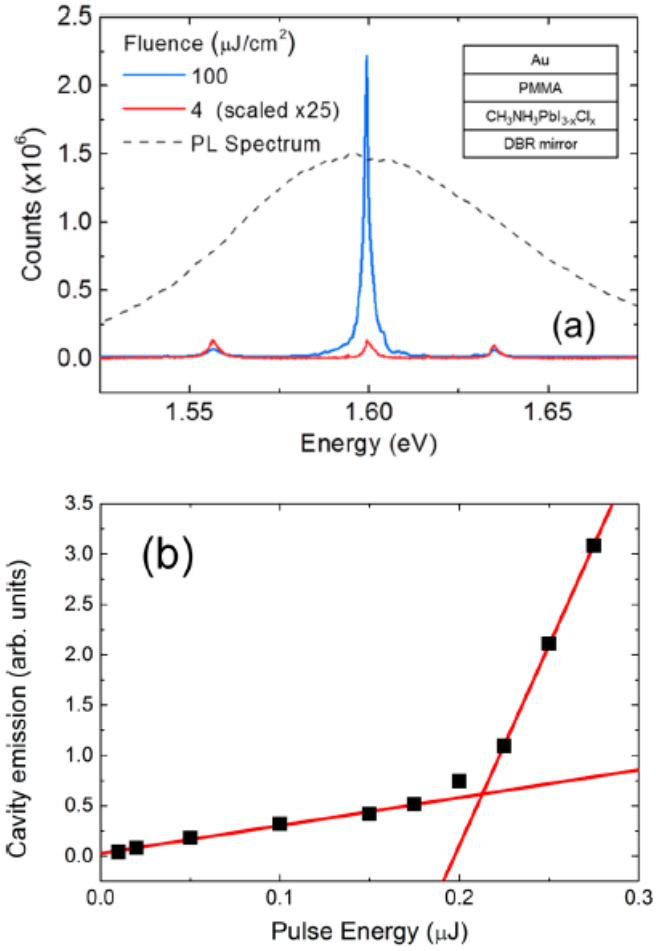

Figure 6: An example of (a) linewidth narrowing and (b) a significant increase in power of a laser system [8].

2.2 Examples of Optical Micro-Cavities

2.2.1 Photonic Crystal Cavity

Photonic crystals (PhC) and photonic crystal cavities (PhCC) briefly played a significant role in the research done for this thesis, but the direction of this research has since moved away from photonic crystals. For this reason, the background information presented here on the PhC is brief. Entire books have been written about the PhC, and the applications of the PhC continues to be a forefront for research in nanophotonics and silicon photonics. Bountiful information is available from textbooks [19]–[21]. I also advise referring to the early PhC research by Eli

Yablonovitch and Sajeev John. Their two landmark papers outlined the physical principles that are fundamental to PhC operation, and kick-started significant research in the area which is made evident by the more than 25,000 citations these two papers have combined [22], [23]. Finally, it is extremely beneficial to understand electronic semiconductors. The physical principles of the electronic semiconductors and the PhC are analogous to one another in many ways.

A PhC structure is a periodic arrangement of two materials of different dielectric permittivity. Each interface of the material gives rise to a small partial reflection of incident radiation, which can lead to the coherent backscattering of light of particular wavelengths. This principle is known as *distributed feedback* (DFB). This opens up a gap in the photonic density of states (DOS); the so-called *photonic bandgap*. This bandgap implies that light of suitable wavelengths is forbidden to propagate through the PhC. However, the implications are more profound on a quantum mechanical level. The bandgap in the DOS gives rise to an inhibition of spontaneous emission for gain materials coupled to the PhC. If there exists an overlap in the photonic bandgap of the PhC, and the electronic bandgap of a gain material, then the creation of photons in the photonic bandgap is forbidden [23]. Therefore, not only is the propagation of inner-bandgap light forbidden by DFB, but the creation of inner-bandgap light is forbidden by the elimination of available states. Introducing a defect within the crystal by breaking its periodicity can allow inner-bandgap photons to be strongly localized to the defect [22].

The study of DFB predates the study of the PhC, and the one-dimensional case can be modeled using classical electromagnetic theory. This principle relies on the interference of backscattered light from a series of interfaces between two materials of different permittivity. Suppose one wishes to block light of free-space wavelength λ_0 from propagating through a material by utilizing DFB. This is equivalent to forcing all backscattered light to interfere

constructively. To do this each material layer should be a quarter-wavelength long. In this case, the round-trip path distance in each material causes a π phase shift. Since one of the reflections is from a low-to-high index interface, there is an additional π phase shift introduced at one interface. Therefore, the net phase shift is a multiple of 2π, so the backscattered light interferes constructively. It is important to note that this quarter-wavelength is within the material, so the index of refraction of the material must be considered. This leads to the condition on the individual material layers.

$$d_{layer} = \frac{\lambda_0}{4n_{layer}} \tag{2.19}$$

where n_{layer} is the index of the material layer. It is more common to define this condition using the *Bragg condition*, given in the following equation:

$$2n_{eff}\Lambda = m\lambda_{Bragg} \tag{2.20}$$

where n_{eff} is the effective index of the periodic structure, Λ is the periodicity of the layered structure, m is a positive integer, and λ_{Bragg} is the wavelength that will be optimally reflected by the layered structure. This wavelength is also known as the *Bragg wavelength*. This Bragg condition is more general than the previously asserted condition that each individual layer must be a quarter-wavelength long. Instead, the period of the layered structure must be a half-wavelength of the effective wavelength in the material. In other words, the individual material layers being a quarter-wavelength long is sufficient, but not necessary for creating constructive interference in the back-scattered waves.

The Bragg condition is dependent on the dimensions in which the structure is periodic. In the one-dimensional case, such as for a distributed Bragg reflector (DBR) mirror, the photonic bandgap only exists for light (or a vector component of the light ray) that is travelling in a direction perpendicular to the material interfaces. If the same periodicity exists in two or three

dimensions, then the same photonic bandgap will exist in each direction. If multiple dimensions exhibit the necessary periodicity, then the photonic bandgap is independent of the direction of light propagation in any component of the periodic medium.

By breaking the periodicity of a PhC, one can introduce a defect state within the photonic bandgap [22]. This break in the crystal's periodicity is the PhCC. A photon of suitable inner-bandgap wavelength can exist in this defect, and will be confined within the defect by the DFB mechanism of the surrounding crystal. The strong localization of this field both temporally (high Q factor) and spatially (low mode volume) gives rise to an enhancement of the gain material's spontaneous emission rate according to the Purcell effect. The *Purcell factor* can be written as:

$$F_P = \frac{3}{4\pi^2}\left(\frac{\lambda}{n}\right)^3\left(\frac{Q}{V}\right) \tag{2.21}$$

Where F_P is the Purcell enhancement factor, λ/n is the wavelength in the PhCC material, Q is the quality-factor of the PhCC resonance, and V is the mode volume of the mode that exists in the PhCC. Thus, a PhCC mode is well-situated for a tightly confined, low threshold lasing mode by virtue of the significantly enhanced spontaneous emission into the cavity mode by Purcell enhancement.

To summarize, there are two important mechanisms that form the working principle of a PhC. The PhC bandgap is created from DFB, which prevents light satisfying the Bragg condition from propagating within the crystal. The introduction of a defect in the PhC gives rise to a resonant cavity (the PhCC) with a narrow DOS spike within the photonic bandgap. This localized spike in the DOS leads to a Purcell enhancement, which describes how a coupled gain medium will exhibit an enhanced spontaneous emission rate into the cavity mode.

In practice, the fabrication of three-dimensional PhC structures operating at optical wavelengths is difficult. It is more common to create a two-dimensional PhC in a dielectric slab.

In this case, light is confined in the direction perpendicular to the slab by total internal reflection. An example of a 2D PhC slab with a nanoscale cavity is depicted in Figure 7, along with a modal profile showing the intense localization of the electric field within the cavity.

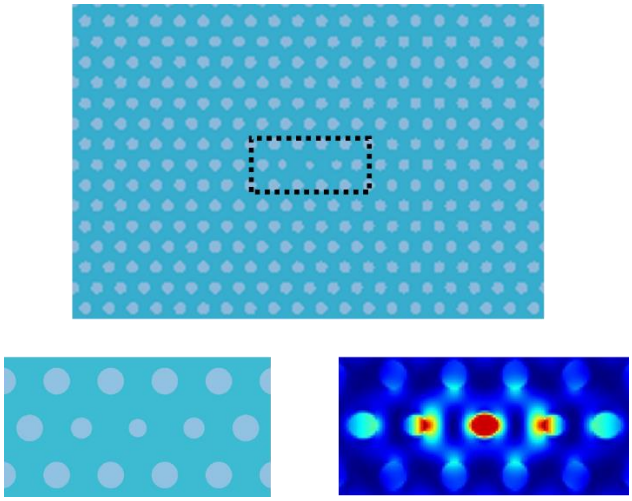

Figure 7: A 2D PhC (top). The region in the dashed line shows a defect in the crystal (bottom left, zoomed), which can function as a high-quality cavity as shown by the localized electrical field intensity in the center hole of the defect (bottom right).

2.2.2 Ring, Disk, and Microtoroid Resonators

The "Whispering Gallery" is a circular balcony in St. James Cathedral in London. It is so called because a whisper can be heard around the entire balcony if someone places their ear near the wall. In the early 1900's Lord Rayleigh and others accurately described the acoustic wave modes in the Whispering Gallery as guided surface waves [24]–[26]. These acoustic wave modes were classified as "Whispering Gallery Modes" (WGM), and arise from acoustic waves propagating along a smooth surface. While the intensity of acoustic wavefronts propagating in an isotropic 3-dimensional medium decay at a rate proportional to the square inverse of distance, a wave that is being continuously guided by a smooth wall will decay at only the inverse of distance [25]. If the wave returns to its original spot with a phase difference that is an integer

multiple of 2π, then the wave will interfere with counter-propagating waves to form a standing-wave resonance.

The WGM phenomenon for acoustic waves exists for electromagnetic waves as well, and has been observed in structures such as spherical dielectric cavities [27], liquid droplets [28], microdiscs [29], and microtoroids [16]. The principle of operation is identical to that of commonly used ring resonators. Light is confined within a smooth, circular material of sufficiently high refractive index. The refractive index contrast at the smooth interface allows light to propagate along the surface via total internal reflection (TIR). The forward and backward propagating waves combine and form a standing wave that fulfills the same resonant condition as its acoustic wave counterpart. An example of a WGM is shown in Figure 8.

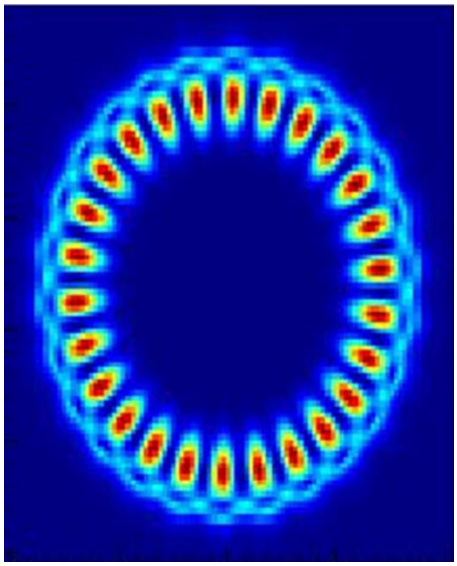

Figure 8: A whispering gallery mode resonance in a dielectric disc. The modal profile was obtained using Lumerical FDTD.

Similar to the Fabry-Perot resonator described in Equation 2.14, the resonant condition of a WGM cavity demands that the total traversed path length of the wave be equal to an integer

multiple of its wavelength. In the case of a circular cavity, the total path length is simply the circumference of the circle.

$$\lambda_0 = \frac{2\pi r n_{eff}}{m} \tag{2.22}$$

where r is the radius of the circle in which the radiation is propagating, n_{eff} is the effective index of the guided mode, and m is a large integer. The fact that m must be large is due to diffraction loss introduced to a WGM that has a resonant wavelength comparable to the size of the cavity. In this case, a significant portion of the energy in the mode is coupled out of the cavity upon each reflection at the surface.

Although this resonant condition is simple, the mathematical modeling of the modal distribution in a WGM is complicated. An analysis of a 2D cylindrical cavity leads to solutions of the wave equation that are transcendental, and can only be solved numerically [30].

Ring, disk, and microtoroidal structures can support WGM with extraordinarily high Q-factors. The Q-factor of these devices can be attributed to four main factors:

$$Q_{total}^{-1} = Q_{mat,abs}^{-1} + Q_{surf,abs}^{-1} + Q_{scatt}^{-1} + Q_{bend}^{-1} \tag{2.23}$$

Each of these terms describes a different mechanism of loss. $Q_{mat,abs}$ describes energy loss due to the resonator material absorption, $Q_{surf,abs}$ describes energy loss due to optical absorption in materials that may have been adsorbed to the surface of the material, Q_{scatt} describes energy loss due to light being scattered out of the cavity for any reason (such as defects, rough edges, etc.), and finally Q_{bend} describes loss that is causes by light being lost from diffraction at tight bends [31].

As long as a WGM features a resonant wavelength that is large compared to the size of the cavity diameter, bending loss is negligible. Silica microstructures suffer from the adsorption of water and various contaminants, leading to a potentially large loss in energy [31]. Scattering

loss represents a practical limitation of disk and ring structures, since the fabrication of these structures does not yield perfectly smooth sidewalls. However, microtoroidal cavities can overcome this practical limitation by utilizing thermal reflow to reshape the cavity into a smooth structure. Furthermore, the circular waveguide on the edge of the microtoroid acts similarly to a spherical resonator, allowing the structure to preserve the ultra-high Q-factors present in spherical resonators while suppressing the mode volume [16]. The Q-factors of silica microtoroid resonators can be on the order of 10 billion, which is near the upper limit imposed by material absorption in silica [31].

The crucial technique utilized to create ultra-high Q-factor microtoroidal structures is the thermal reflow of silica that creates a smooth material interface. This technique was developed by Kerry Vahala and co-workers in 2003 [16]. I will describe that fabrication process now, since a similar technique will be described later in this thesis that could potentially create high-Q perovskite resonators through chemical reflow. The process is also depicted in Figure 9.

First, a layer of SiO_2 is deposited on a silicon wafer. It is then patterned by standard photolithography into a large, 160 μm diameter circle. The SiO_2 pattern is then partially undercut by an isotropic Si etch in XeF_2. At this point, there is a SiO_2 disc resting on a pedestal of Si. However, the fabrication thus far will undoubtedly leave blemishes in the SiO_2 disk that will limit its performance as a WGM resonator. The final step is to use a CO_2 laser to reflow the thermally isolated disk periphery. This final step enhanced the Q-factor of the device from $\sim 10^5$ to $\sim 10^9$.

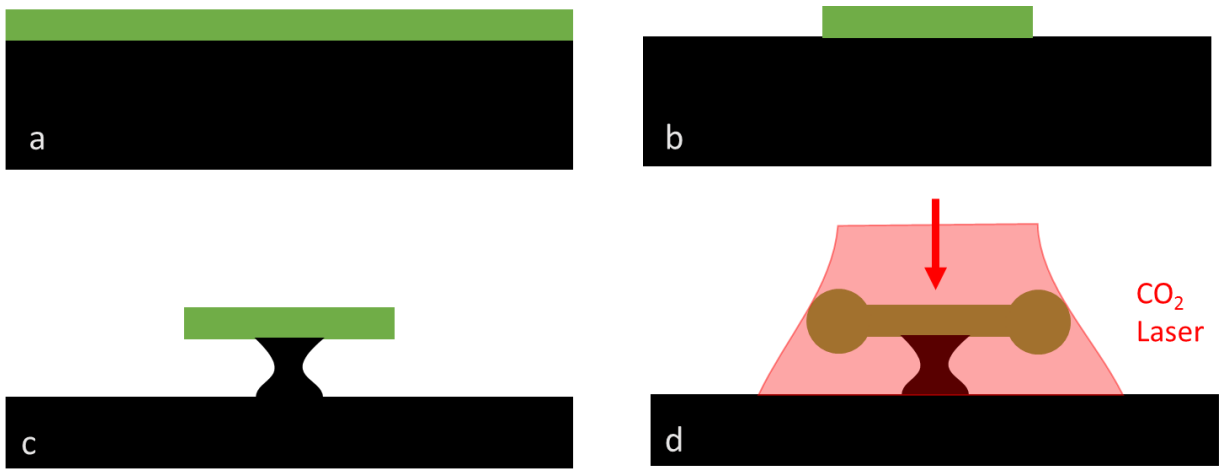

Figure 9: Fabrication of a silica microtoroid by thermal reflow. (a) A SiO_2 layer is deposited on Si. (b) The SiO_2 layer is patterned by photolithography. (c) The silicon is etched isotropically using XeF_2. (d) The SiO_2 disk is illuminated by a CO_2 laser, allowing the edges to reflow.

Chapter 3. Design of Photonic Crystal Cavity and Patterning of Silicon Nitride Membrane

3.1 Initial Motivation: Optically Trapping Cells in a Microfluidic Channel

Presented in this chapter are the methods I used to optimize a PhCC in simulation, and some of the subsequent fabrication steps that were taken to realize such a structure. While the idea of coupling a perovskite gain medium to the cavity is a direction that may be taken, the design of this particular structure was done with a different project in mind. This project idea will be briefly described here, since the nature of the project influenced the various design parameters of the PhC.

The project sought to trap a cell via evanescent coupling from the cavity mode to the cell located directly above the PhC plane, as is shown in Figure 10. This was an extension of the project described in [32], and its aim was to replace the large external trapping laser with an on-chip PhC light source integrated beneath a microfluidic channel. In order to know the exact placement of the cell on the PhC platform, it was beneficial to make the cavity comparable to the size of the cell. This choice dictated the cavity dimensions for this design, but it should be noted that a much larger Q-factor can be obtained by increasing the length of the cavity.

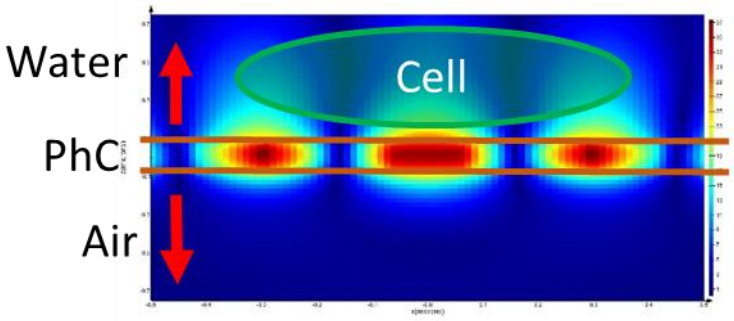

Figure 10: Side-view of a PhC slab. The localized electric field in the PhCC can exert an evanescent trapping force on the cell.

Evanescent waves decay over a small spatial distance, which is on the order of the wavelength of light in the medium. In order to couple enough light to exert a sufficient optical force on the cell, it is desirable to place the microfluidic channel as close to the optical cavity as possible. For this reason, we sought to use single-molecule thick WSe_2 as a gain medium. The peak photoluminescence of monolayer WSe_2 is at approximately 740 nm, so the PhCC was designed to resonate at this wavelength [33].

More information regarding optical trapping can be found in Ref. [34]. After discussing the details of this particular PhC in Section 3.2 and Section 3.3, I will discuss how this work can be extended to include the perovskite micro-cavity laser project in Section 3.4.

3.2 Design and Simulation of a Silicon Nitride Photonic Crystal Cavity

This section discusses the design of a particular PhC, and will focus primarily on the simulation instead of general theory. A more detailed discussion of the working principles of the PhC is discussed in Section 2.2.1, but various parts of that discussion are reiterated here when they have an influence on the design choices made for this particular structure. It should be noted that the designed structure has not yet been realized through fabrication, and it is reasonable to speculate that the simulated structure may not perform well when all fabrication errors are taken into consideration. These issues, along with suggested future directions are discussed in Section 3.4.

3.2.1 Design Considerations

There are many design choices one needs to make to create a PhC with a desirable bandgap, and a PhCC cavity with a high-Q resonance at the desired wavelength. These choices can be boiled down to two categories: material consideration, and pattern considerations.

As with any optical resonator, the materials that the resonator is made of must be transparent at the desired resonant wavelength. If this is not the case, then absorption will decay the resonance quickly, and the Q-factor will be lowered. Another material characteristic that governs the performance of a PhC is the index of refraction. A PhC forbids the propagation of light within the photonic bandgap via partial reflections induced at material interfaces. This distributed Bragg reflection gives rise to a photonic bandgap only if the index contrast between the two PhC media is sufficiently large.

While Bragg reflection is responsible for the propagation and confinement of light within the plane of the PhC, TIR is responsible for the confinement of light in the direction perpendicular to the surface of the PhC. Since TIR also requires a sufficiently large index contrast at the material interface, the required index contrast is necessary for confinement in all three dimensions.

The final material restriction is that the material is able to be patterned at the nano-scale. Optimal PhC feature sizes can be as small as tens of nanometers, and must be very smooth to prevent scattering from surface defects. In some cases, this restriction applies to only one of the materials. For instance, Chen *et al.* created a PhC structure by patterning glass, and spinning perovskite over it [6]. While perovskite is a difficult material to pattern lithographically, the patterned glass was sufficient to create a PhC structure.

To summarize, the three main material consideration for a PhC design are:

1. The materials must be transparent at the desired wavelengths.
2. The index of refraction contrast between the two materials must be sufficiently large.
3. At least one of the materials must be capable of being patterned at the nano-scale.

Some materials that satisfy these criteria are SiN, and gallium phosphide (GaP). Both are transparent at 740 nm and are capable of being patterned at the nano-scale [33]. The refractive index of GaP is approximately 3.1, while SiN can be anywhere from 1.9 to 2.3 depending on the fabrication method. While GaP is clearly a better choice as a high-index medium, SiN has other advantages. It is silicon-based, and can therefore be simply integrated with other silicon-based structures such as the one reported in [32]. It is also inexpensive, and its fabrication procedures are better characterized at the Washington Nanofabrication Facility (WNF). For these reasons we chose SiN as the starting material for this design, but also recognize that GaP is the better choice if the low refractive index ends up crippling the SiN PhC design.

SiO_2 also satisfies criteria 1 and 3. It is transparent at the desired wavelength, and is capable of being patterned at the nano-scale. However, it has a very low refractive index. Since PhC structures involve a material of high index and a material of low index, SiO_2 can be used as the low index material. This is how the PhC in [6] functioned.

The second group of design choices one must make involves the PhC pattern itself. Fortunately, due to the maturation of this field over the past couple decades one can often find a pre-existing structure that has already been demonstrated to work. Since SiN PhC structures have been created before, one can use these structures as a template and make only minor changes to obtain an optimal structure. PhC structures are scalable to the extent that the absorption and dispersion characteristics do not change significantly, so a SiN PhC can be scaled to shift the photonic bandgap to whatever is needed in the optical regime.

Although it is useful and efficient to begin a design using a pre-existing structure as a template, it is also very useful to understand some basic design criteria. For optimal confinement

in the direction perpendicular to the PhC plane, the thickness of the PhC should be approximately half the wavelength:

$$t \cong \frac{\lambda_0}{2n} \tag{3.24}$$

where λ_0 is the free-space wavelength, and n is the refractive index of the PhC slab.

The theory of a one-dimensional distributed Bragg reflector does not perfectly extend to two dimensions in practice, but it allows us to find an approximate initial value for both the lattice constant spacing, *a*, and the radius of the holes in the PhC, *r*. This is discussed in section 2.2.1.

The choice of a hexagonal lattice of holes was completely based on past literature [35], [36]. Supposedly this arrangement yields the largest photonic bandgap, but I have not simulated other lattice types to verify this myself.

With these criteria in mind, a simple PhC structure can be simulated using a numerical *finite-difference time-domain* (FDTD) solver, such as Lumerical FDTD. To optimize the band structure of the PhC, I swept the thickness, lattice constant, and radius of holes to achieve a large bandgap. I did not try to optimize the exact location of this bandgap to the desired wavelength, but instead focused solely on widening the bandgap as much as possible through a systematic, iterative process of sweeping each parameter independently. These sweeps serve to shift the individual parameter to a roughly approximate optimal region, but since the parameters in the PhC design are not completely independent from one another it is very difficult for these independent sweeps to converge to the optimal solution. It is therefore necessary to take an additional step, and optimize all of the parameters simultaneously.

This final optimization step can be done using Lumerical FDTD's built-in optimization algorithm, which closely mimics standard genetic algorithms for optimization. It is a

computationally-taxing technique, and requires a lot of time to converge to an optimal solution. By first performing individual parameter sweeps, one can narrow down the search-space for each individual parameter during the combined optimization, and thus reduce the required time and memory significantly.

Once this final optimization is done, we can assume the bandgap is as large as possible for the particular wavelength it is centered at. It should be noted that widening the bandgap like this is not always a necessary step, and is sometime undesired. Since we aimed only to widen the bandgap without paying any attention to the desired wavelength ($\lambda_{desired}$), the optimization may have created a bandgap centered on an undesirable wavelength ($\lambda_{current}$). Since PhC structures are scalable by wavelength, we can now scale all features of the PhC using Equation 3.25:

$$S = \frac{\lambda_{desired}}{\lambda_{current}} \tag{3.25}$$

where S is the scaling factor for each dimension.

In reality, scaling is not perfect, and it can be beneficial to repeat this process described to widen the bandgap at the newly located wavelength. Another issue with scaling arises from the inability to scale certain parameters. Most notably, if one purchases a commercial wafer with a nitride layer, the thickness is often fixed. However, it is still best to scale all of the other parameters while keeping the thickness fixed, followed by a reoptimization. This process is summarized in Figure 11.

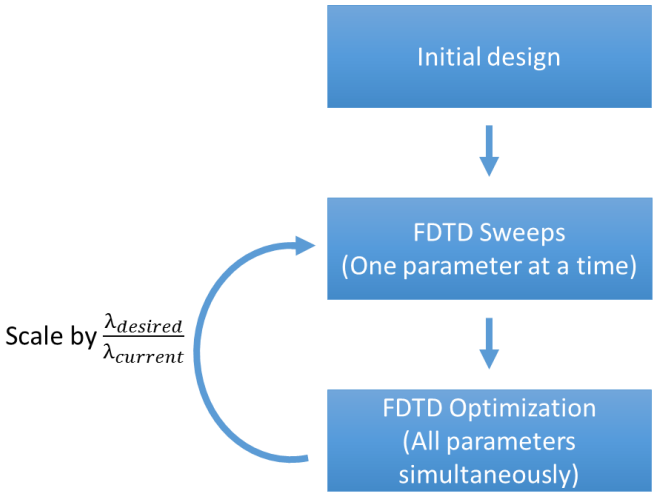

Figure 11: Numerical simulation process flow for optimizing a PhCC design.

After the photonic bandgap is optimized, we can now introduce a defect into the PhC which we call the PhCC. This defect is a region where the periodicity of the PhC is broken, thereby introducing a state within the photonic bandgap such that photons of a particular wavelength can exist locally.

As described in Section 3.1, the light confined in the PhCC should be of comparable size to a cell. The cells we intended to trap were a few microns long. The cavity we chose for this was an *L3 cavity*, which is a defect introduced by filling in three adjacent, collinear holes. Various form of this sort of structure are shown in Figure 12.

It has been reported that the quality factor of a PhCC can be improved by implementing a tapered design, in which the radii and placement of the holes in the defect are gradually altered, rather than the holes being completely removed [37]–[39]. This sort of structure still breaks the periodicity of the PhC in a fashion similar to that of an L3 cavity. A depiction of how each of the previously described steps increases the Q-factor of the cavity is shown in Figure 12.

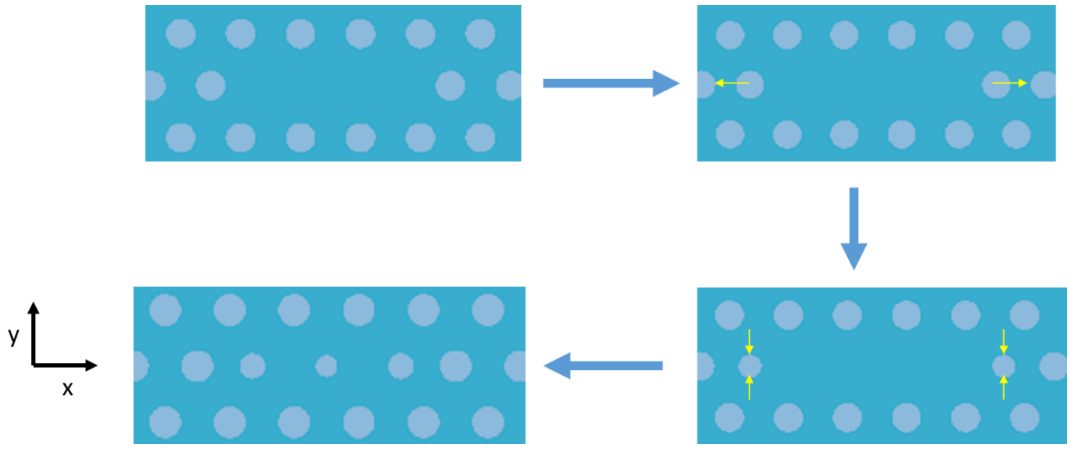

Figure 12: Development of an L3 cavity. Each step enhances the Q-factor of the cavity. For specific dimensions, see Figure 13.

The final structure is an “L3-like” cavity. It is similar to an L3 cavity in that three adjacent, collinear holes are altered to break the periodicity of the PhC, but is different in that it implements a tapered design instead of completely removing the holes.

The PhCC Q-factor can be optimized in a similar way to the PhC bandgap, following the same process flow as in Figure 11. The most critical parameters to adjust are the cavity hole displacements and radii, since the bandgap of the surround PhC should already be optimized.

After optimization, this structure has a Q-factor of ~5000. However, this value will most likely drop by perhaps a couple orders of magnitude due to fabrication tolerance, but I have not tested this. Furthermore, the simulated Q drops by a factor of ~10 when the PhC is placed directly under a microfluidic channel filled with water, which would be the case if this structure were used in cell-trapping applications. The final device parameters and results are summarized in Figure 13.

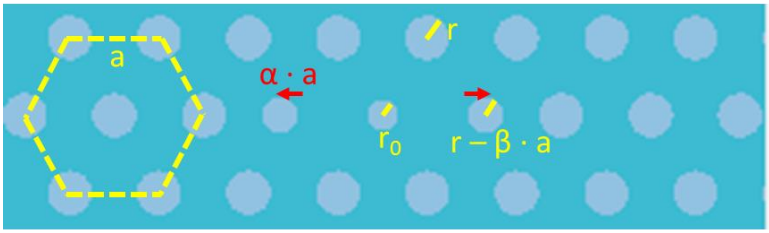

Parameter values	
a	329 nm
r	81 nm
r_0	55 nm
α	0.15
β	0.05
t	165 nm
Q	~5000

t: layer thickness
Q: quality factor

Figure 13: The designed PhCC, with corresponding parameter values.

3.3 Fabrication

Here I will describe multiple fabrication procedures. Two approaches were taken for patterning a PhC in SiN, both unsuccessful due to issues with etching. I will explain these fabrication processes in detail, and explain why they failed. After these attempts, we directed our focus towards characterizing a plasma etch on a SiN membrane. This fabrication utilized photolithography instead of electron-beam lithography (EBL), and resulted in the successful patterning of various test features. The results of this are a promising step towards fabricating a PhC structure directly on a SiN membrane. Various unsolved issues and suggested future tests are discussed in Section 3.4.

3.3.1 Photonic Crystal on PECVD Silicon Nitride

There are two common ways of depositing SiN. The first is plasma-enhanced chemical vapor deposition (PECVD), the second is low-pressure chemical vapor deposition (LPCVD). PECVD results in a non-stoichiometric film of perovskite, often times chemically denoted as

$Si_xN_yH_z$ to express the variability in chemical composition of the film and the significant atomic percentage (>10 %) of hydrogen that can invade the membrane during the deposition [40]. LPCVD results in a so-called stoichiometric film, which is far purer and denser compared to PECVD SiN.

Two significant effects arise from the differences in these films. Because LPCVD nitride is denser, the refractive index can reach upwards of 2.3. The index of refraction of PECVD nitride is less, and was approximately 2.0 in our case. The difference in densities can also lead to significantly different etch rates, with LPCVD nitride generally being more resilient than PECVD nitride. In particular, there exists a profound difference in the etch rates in potassium hydroxide (KOH), in which PECVD nitride etches at ~0.67 nm/min while LPCVD nitride does not measurably etch in KOH [40]. The high etch rate of PECVD is what ultimately made this fabrication process a failure, as the final step of the fabrication requires a release of the SiN membrane in a KOH wet etch. During this wet etch, the features on the SiN membrane are destroyed.

The fabrication process is schematically depicted in Figure 14. First, PECVD SiN is deposited on both sides of the chip, followed by a PECVD SiO_2 deposition on the back. Windows in the SiO_2/SiN layers are then etch on the back. On the top-side, a thin 20 nm layer of titanium is evaporated onto the SiN. This serves as a charge-dissipation layer during EBL, which is often needed when writing patterns on an electrically insulating layer. If the substrate material is non-conductive, then charge can accumulate in the layer and deflect the electron beam. Next, ZEP EBL resist is spin-coated onto the titanium, and subsequently patterned via EBL. The pattern is transferred to the SiN layer using an ICP-RIE CHF_3/O_2 etch chemistry, and the ZEP is

removed using dichloromethane (DCM). Finally, the membrane is released by etching the underlying Si in KOH.

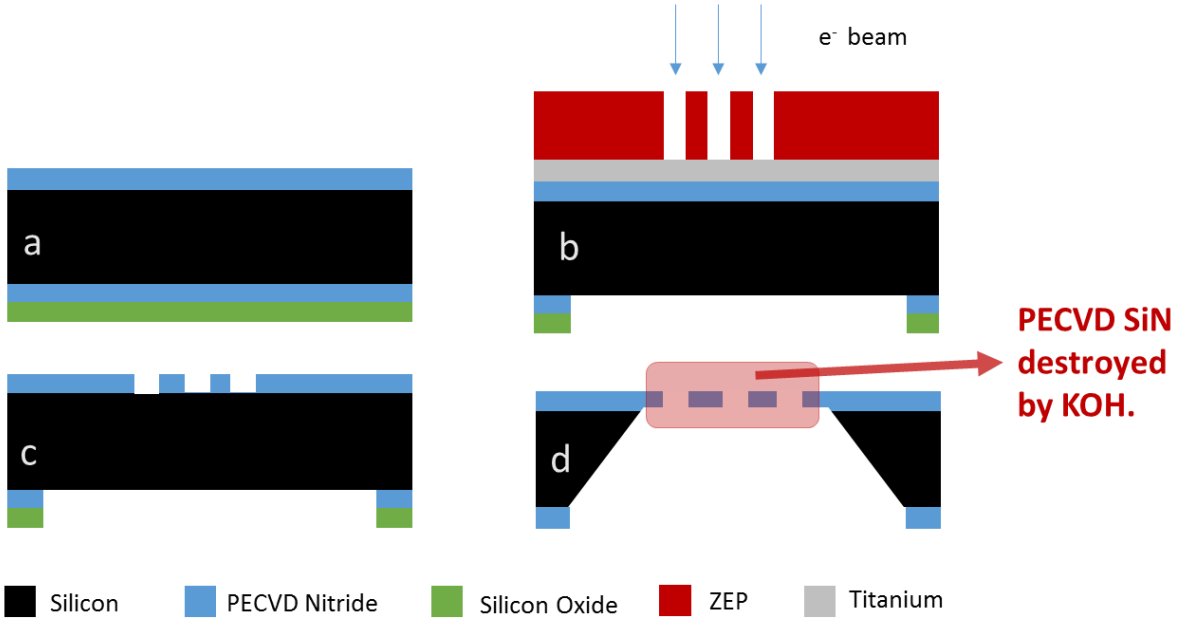

Figure 14: a) PECVD nitride is deposited on both sides of a silicon wafer, and PECVD oxide is deposited on the backside. b) The backside oxide and nitride films are patterned with photolithography and etched via RIE. A 20 nm layer of titanium is deposited on the top to serve as a charge-dissipation layer during EBL. 300 nm ZEP resist is spin-coated on the top, the PhC pattern is written with EBL, and developed in amyl acetate. c) PECVD nitride is etched via ICP-RIE, and the ZEP is removed in DCM. d) The top PECVD nitride layer is release in a wet KOH etch. The process etches away the glass on the backside, as well as the silicon wafer. In the case of PECVD nitride, the top nitride layer is unfortunately destroyed in the process.

3.3.2 Photonic Crystal on LPCVD Silicon Nitride Membrane

A way to avoid the issues from the PECVD nitride fabrication in Section 3.3.1 may be to use LPCVD nitride, changing only the step in which the SiN film is deposited. However, we decided to pattern a released SiN membrane directly, instead of releasing the structure at the end of the process. This method draws upon the commercial availability of high-quality, low-stress

LPCVD nitride membranes. Creating these membranes is not a straight-forward process, and purchasing high-quality membranes eliminates the need for us to facilitate and characterize the fabrication ourselves.

The fabrication method is depicted in Figure 15. The SiN membrane chips were purchased from Norcada (Part No. NX5050D). The thickness of the SiN layer is 200 nm, and the membrane is a 500 μm square. A 300 nm layer of ZEP was spin-coated on the chips, and the PhC pattern was subsequently written via EBL. Since patterning on SiN membranes is not a well-documented process, it was necessary to expose the pattern at different dosages to find the optimal dosage. A sample picture of this "dosage matrix" is shown in Figure 16. The pattern in that figure is not the PhC pattern, but rather a large test pattern written via EBL.

Following the development of ZEP in amyl acetate, the PhC pattern was transferred to the SiN membrane using ICP-RIE. During the etch, the silicon carrier wafer was cooled to 10 Celsius. The CHF_3 flow is 26.0 sccm, and the O_2 flow is 1.0 sccm. The chamber pressure is 5.0 mTorr, the RF forward power is set to 25 W for the RF generator, and the RF forward power is set to 2250 W for the ICP generator. Following the etch, the ZEP and titanium was then stripped in Piranha solution, and the final pattern was imaged in an SEM.

One of these SEM images is shown in Figure 17. This image shows that something clearly went wrong in the process. Stylus profilometry (Alpha Step 200) performed on a feature written off the membrane shows that the thickness of the nitride film decreased from 200 nm to ~70 nm. This means that the ZEP resist was entirely etched away, leading to the entire SiN film being etched for a period of time. Another image of a chip undergoing the same process is shown in Figure 17. In this process, the SiN membrane was completely destroyed during the ICP-RIE etch.

From these chips we hypothesized that the failed fabrication was due to excessive heating during the etch step, and we shifted our focus towards characterizing the etch process. This characterization is described in the next section.

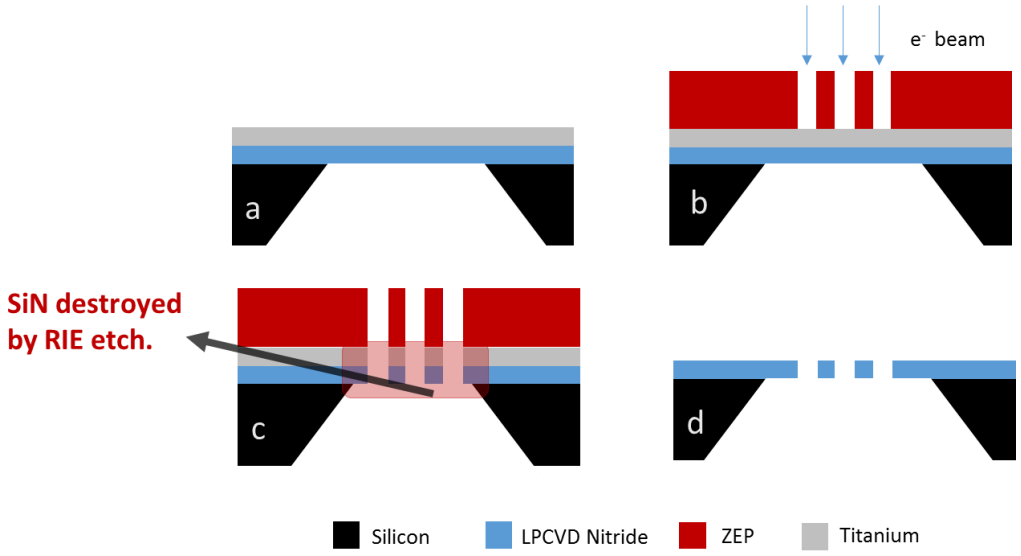

Figure 15: (a) Starting with a commercial SiN membrane, a 20 nm titanium layer is deposited via electron-beam evaporation. (b) ZEP e-beam resist is spin-coated on the chip, and is patterned by EBL. (c) Titanium and SiN are ICP-RIE etches, resulting in the SiN membrane being destroyed. (d) The ZEP and titanium are removed in Piranha solution.

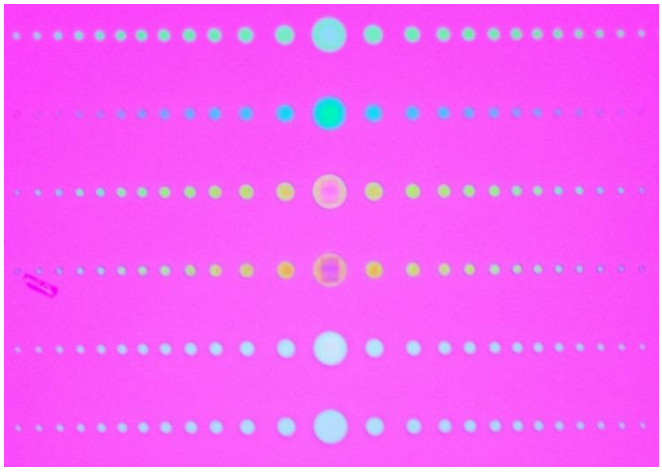

Figure 16: An example of a "dosage matrix" written in ZEP. Each row was written at a different dosage. The top five rows are written at a dosage that is too small for proper development. The bottom row is written at the proper dosage.

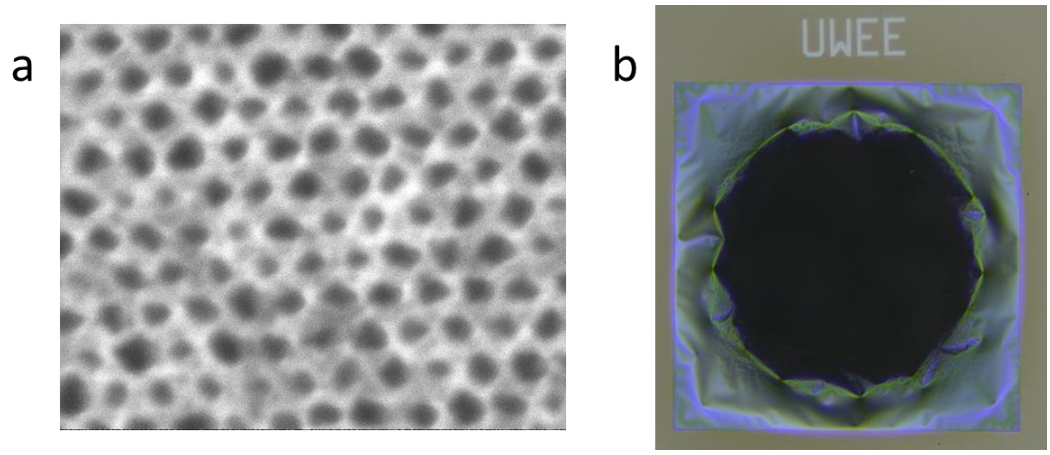

Figure 17: (a) A PhC pattern that is severely distorted due to excess heating during the SiN etch process. (b) A SiN membrane that was destroyed during an etch process.

3.3.3 Photolithographic Test Structures on LPCVD Silicon Nitride Membrane

It is very important to keep a structure cool during a plasma etch, since etch rates can vary significantly with temperature. When etching a wafer in the Oxford ICP-Fluorine etcher at the WNF, the edges of the wafer are cooled with liquid nitrogen. If one wishes to etch a small chip, the chip is mounted to a carrier wafer with Fomblin oil to facilitate thermally conductive contact between the chip and the cooled wafer. Furthermore, the etch process can be broken up into multiple intervals such that the structure is etched for only a few seconds at a time, and then allowed to cool. For these SiN chips, using both Fomblin oil to mount the chip and etching for 7 second intervals still resulted in unpredictable etch rates, and often times a membrane that was destroyed in a similar manner to the one shown in Figure 17b.

I hypothesize that the reason for this unpredictability results from a temperature gradient on the SiN membrane that causes an increased etch rate of the membrane and the resist layer above it. While the Fomblin oil most likely keeps the silicon frame of the chip cool, there may still exist poor heat conduction from the SiN membrane to the cooled carrier wafer due to the

low thermal conductivity of SiN. If this is the case, then the temperature of the membrane would be highest at its center and would decrease with radius. This may explain why the destroyed membrane in Figure 17b has a roughly circular hole in it. SiN can withstand very high temperatures, so it is highly unlikely that the membrane is melting or being fractured by thermal stress.

Based on this hypothesis, I adjusted the fabrication by adding a 100 nm aluminum layer on the backside of the chip with the hopes that it would provide thermally conductive contact between the membrane and the cooled silicon frame. In order to make measurements easier, and to minimize the cost of fabrication, photolithography was used to pattern the membranes instead of EBL. The fabrication is summarized in Figure 18.

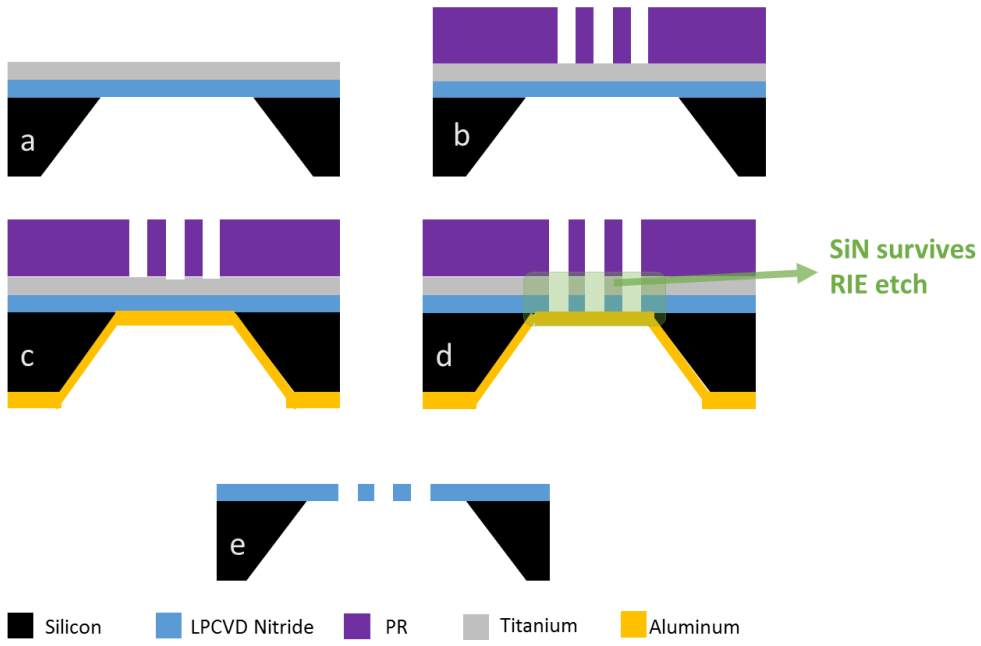

Figure 18: Fabrication process for etching features into a thin nitride membrane. This is identical to the fabrication shown in Figure 17, except (b) AZ1512 photoresist is patterned with photolithography and (c) an aluminum layer is deposited on the backside of the chip.

With the addition of this aluminum layer, I was able to fabricate multiple chips with various feature sizes in a predictable and repeatable way. One such chip is shown in Figure 19. Optical profilometry was used to measure the step heights of partially-etched features on the SiN membrane, showing that there was no measurable gradient in the etch rate. This is shown in Figure 20. It was clear from visual inspection under a microscope that the photoresist layer was not entirely etched away.

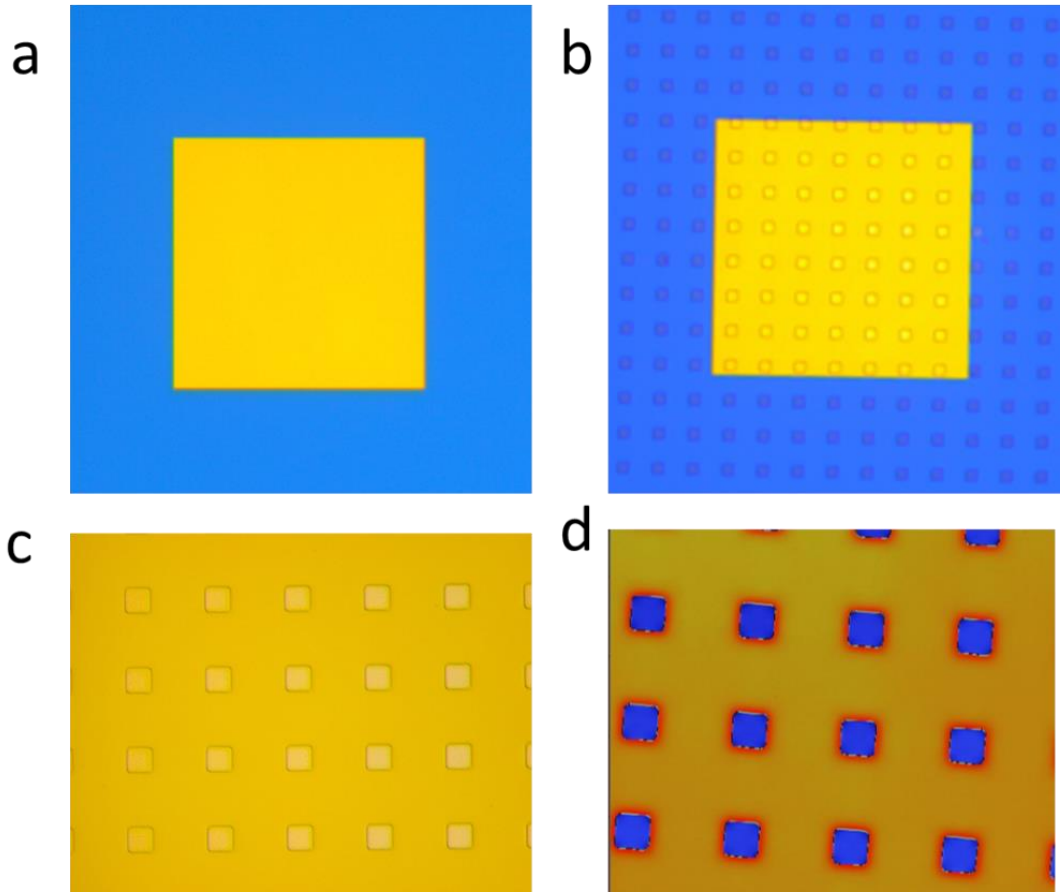

Figure 19: (a) An unpatterned 200 nm SiN membrane. The blue is SiN on top of the Si substrate, and the orange is the SiN membrane. The color of the layer arises from thin film interference, and is therefore dependent on film thickness and the underlying material. (b) A SiN membrane chip patterned with a grid of partially etched 20 μm squares. (c) Zoomed in image of the patterned SiN membrane with a (d) corresponding topology measurement showing the uniformity of etch depths on the membrane.

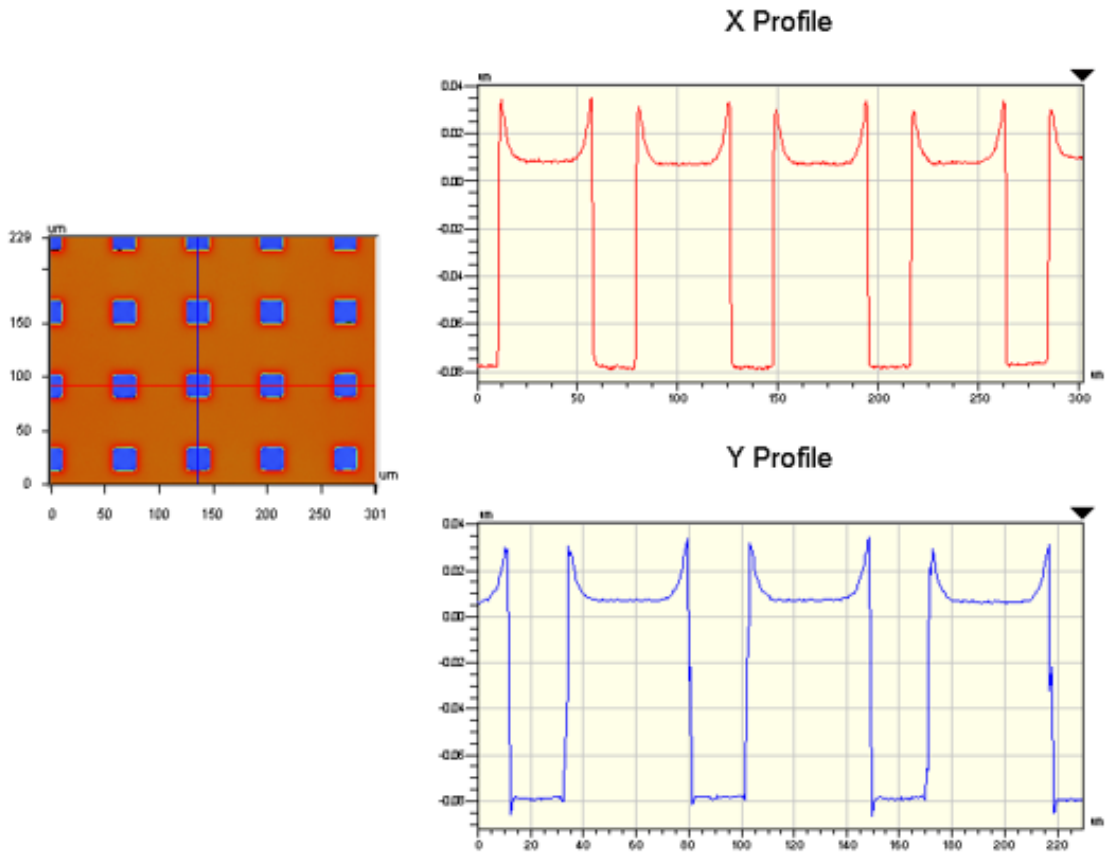

Figure 20: Optical profilometry measurment of the surface profile of patterned SiN membranes. This was performed on the Wyko NT3300 profilometer at the WNF.

3.4 Unresolved Issues and Future Directions

Although the fabrication of test structures on the SiN membrane was done successfully, the features were large. It is unclear to me whether there will still be an issue when nano-scale features are being etched. Furthermore, my hypothesis that the issues with the etch stemmed from excessive heating of the membrane is still not proven. If this etch technique is emphasized in any future work, I suggest modeling heat transfer in membranes in simulation and in theory to verify if heating is indeed an issue.

The designed PhC was for the purpose of trapping a cell, and at the time of designing the intended gain medium was monolayer WSe_2. WSe_2 has a peak a PL of ~740 nm. This

wavelength is very close to the peak PL of perovskite at ~780 nm, and therefore the PhC can easily be scaled by ~780/740 to obtain a structure that is near-optimal.

I have significant doubts as to whether this design will work after all fabrication errors and tolerances are taken into consideration. One way to verify this is to simulate a slightly roughened PhC structure, or one in which the holes vary in radius slightly. However, these sorts of simulations break the periodicity of the structure, which increases simulation time and memory by a factor of 8. I suggest redesigning the structure to increase the size of the cavity. Since the original project sought to trap a cell, the optical cavity was designed to be very small. The quality factor suffers with the reduced spatial confinement. Increasing the cavity length by removing/modifying more holes will increase the Q-factor drastically.

Should these design changes not be sufficient for a perovskite laser, the next step is to move to a higher index material. GaP has a much higher index than SiN, and is better-suited for confining light via Bragg reflection and TIR. The bandgap of a SiN PhC is very narrow due to the low refractive index contrast between SiN and air. Considerable effort was spent in trying to widen this bandgap, however a wide bandgap may not always be beneficial for lasing. If one uses GaP, then the bandgap can be much larger than SiN, and the designer may need to narrow the bandgap such that it only encompasses a small region around the desired lasing wavelength.

If a high-Q PhC is indeed fabricated, then the next issue will be coupling perovskite to the cavity. Spin-coating perovskite on the structure will completely alter the performance of the PhC, since the air holes would now be filled with perovskite. This adverse effect would exist for both the SiN and the GaP cavities, since the refractive index contrast between those two materials and perovskite are roughly the same (SiN is ~2.2, perovskite is ~2.7, and GaP is 3.1)

[33]. It should be noted that if perovskite coats the entire SiN PhC, then perovskite will be the high index material, and will thus contain the lasing mode.

A promising direction may arise from looking into a lift-off process using ZEP resist and evaporated perovskite. A challenge here is finding a method of evaporating perovskite. Dual-source evaporation has been described in literature, but I do not know of any group on the University of Washington campus that uses such a deposition technique [41]–[43]. If one has the capability of evaporating perovskite, then it may be simple to pattern ZEP on top of the PhC, deposit a layer of perovskite via directional evaporation, and perform a lift-off process in DCM. The effects of DCM on perovskite should be further investigated if this route is chosen, especially since the properties of evaporated perovskite may be different than those of spin-coated perovskite.

Chapter 4. Design of Whispering-Gallery Mode Laser

4.1 Chemical Reflow of Perovskite Thin Films

WGM lasing modes can exist in smooth round structures, such as rings, discs, and microtoroids. In an attempt to create such a smooth structure, we first tried directly patterning perovskite with EBL, which is discussed in more detail in the next section. The resulting structures had very rough side walls, with significant roughness being visible in optical microscopy. A WGM laser relies upon the side walls being very smooth to prevent scattering losses, so we predict that the fabricated structures would not be capable of harboring a WGM. In an effort to smoothen out the structures, we were led to an active field of research in photovoltaics regarding the post-deposition treatment of perovskite thin films.

Research in perovskite photovoltaics is actively searching for ways to enhance the quality of thin-film perovskite. Spin-coated perovskite is susceptible to pin-hole formation, low crystallinity, and phase inhomogeneity that adversely affect carrier transport characteristics and make the fabrication of high-quality films a challenge [4]. To address the imperfections of the deposition, some research is focused on post-deposition treatment of spin-coated perovskite films [3], [4].

A method introduced by Zhou *et al.* in 2015 utilizes a reaction between CH_3NH_2 (methylamine, or MA) vapor and $CH_3NH_3PbI_3$ perovskite [3]. When the MA vapor is introduced, an intermediate $CH_3NH_3PbI_3{\cdot}xCH_3NH_2$ liquid phase occurs which allows the film to spread and remove defects in the film [3]. Upon removal of the MA vapor source, the perovskite thin film rapidly recrystallizes into a solid film. Zhao *et al.* further characterized this post-deposition MA treatment, showing that the treated perovskite film can have an enhanced power conversion efficiency (PCE) of ~9% [4].

The increase in efficiency of the solar cells reported by Zhao *et al.* may not imply that the light-emitting properties of the perovskite thin film are similarly improved. It is concluded that the enhanced PCE does not stem from the elimination of non-radiative recombination pathways, but more likely from removal of macroscopic defects such as pin-holes that limit film coverage. Other interesting phenomenon arise from this treatment, such as a ~7% blue shift in the peak PL, and a slight reduction in peak PL power. It is not completely clear if this treatment will significantly affect the material properties of lasing performance, but this is a topic that should be looked into in case there exists a way to enhance lasing performance.

The reason we are particularly interested in this post-deposition treatment of perovskite is not only due to the potential for material enhancement, but primarily due to the liquid intermediate phase of the perovskite film. As described in Section 2.2.2, some of the highest quality optical structures are fabricated by reflowing SiO_2. MA vapor treatment allows for a chemical reflow of perovskite films, which could be used to pattern perovskite into similarly smooth, resonant structures.

4.2 Fabrication and Results

Here I will describe two fabrication attempts. The first was an attempt at directly patterning perovskite via conventional EBL and RIE processes, which resulted in a rough structure that is highly unlikely to be capable of harboring a WGM; the second was an attempt at creating a perovskite microdisc embedded in a smooth glass hole.

4.2.1 Direct Patterning of a Perovskite Thin Film

In order for an EBL process to be compatible with perovskite, the chemicals used in the process must not significantly alter the perovskite film. To test the chemical compatibility of

various EBL process chemicals, I dunked perovskite films in the test chemical for the amount of time that would be necessary in an EBL process. Oftentimes discoloration of perovskite can be clearly seen by the naked eye, indicating that the film has been destroyed. If a chemical did not alter the color of the perovskite film, the film's PL was then measured to check if there were any significant alterations to the light-emitting properties of the film. While more effort can be put into quantifying changes in the thin film, such as XRD analysis, these two tests were the only ones undertaken so far.

The results of this study suggests that perovskite is compatible with anisole, amyl acetate, and dichloromethane (DCM), since the PL spectrum was not significantly altered by these chemicals. If one uses ZEP for an EBL process, then anisole can be used as a precursor, amyl acetate as a developer, and DCM as a stripping solvent, so the entire process can be done without significantly affecting the perovskite with solvents. I did not test the PL after exposure to anisole, but no coloration change was observed. It may be beneficial to the reader to know that toluene, hexane, and methanol do not seem to degrade perovskite, while isopropyl alcohol (IPA), acetone, and water degrade films.

The fabrication process used to directly pattern perovskite with EBL is depicted in Figure 21, and the resulting structures are shown in Figure 22. A 300 nm film of ZEP was spin-coated onto a 1.5 cm x 1.5 cm glass chip with an approximately 200 nm layer of spin-coated perovskite on top. The desired perovskite pattern contains circular pillars, so an inverse pattern was written so that perovskite surrounding the pillars could be etched away. The etch was done using a low-power O_2 RIE etch (Trion Phantom). This recipe is a typical "descum" recipe that is commonly used to etch resists at a slow rate. Although it was unclear from the resulting chips, this O_2 descum etch leaves behind a faint yellow residue of unknown material. While most of the

perovskite film etched in a few minutes, future tests showed that the resulting residue was not noticeably etched after 20+ minutes.

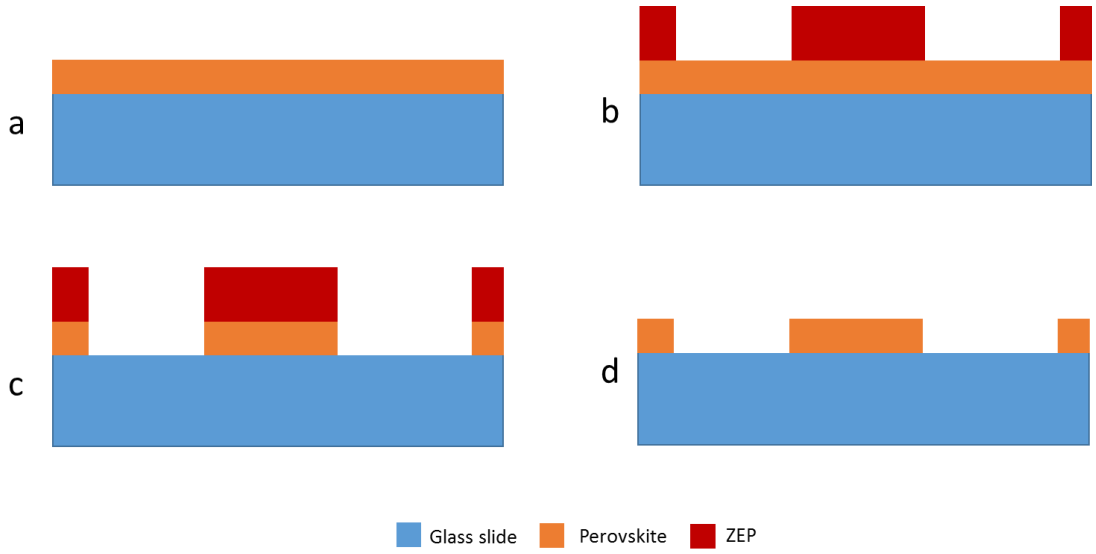

Figure 21: Direct patterning of perovskite using EBL. (a) 200 nm perovskite is spin-coated on a glass slide. (b) ZEP e-beam resist is spin-coated on the perovskite, and is patterned by EBL. (c) The perovskite is etched in an O_2 plasma. (d) The ZEP layer is stripped in DCM.

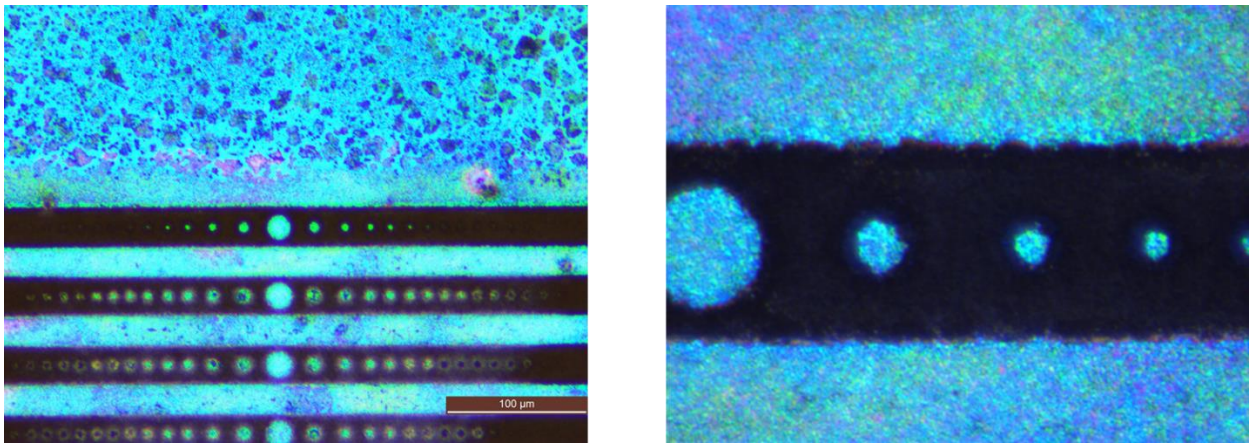

Figure 22: Rough perovskite microdiscs patterned through an EBL and RIE etching process.

Following the RIE etch, the remaining ZEP was stripped in DCM, and the resulting perovskite structures were viewed under an optical microscope. Images are shown in Figure 22.

It is clear that the features are very rough, both on the top and on the sides. No further tests were performed on these patterned structures.

To my knowledge, there does not exist a method that can smoothen out these structures while preserving their general shape. The chemical reflow resulting from exposure to MA vapor results in complete liquid phase change in less than a second. During this liquid phase transition, rapid diffusion of the liquid would most likely cause the patterned structures to join together, leaving a uniform film of perovskite upon recrystallization. If one finds a less aggressive way of reflowing the perovskite, then that method may be used on these structures. Even in such a case, it is difficult to say what the perovskite shapes will look like upon recrystallization.

4.2.2 Fabricating a Perovskite Microdisc Using Chemical Reflow

There are numerous ideas for fabricating a perovskite resonant structure using chemical reflow, and I will discuss the untested ideas in Section 4.3. In this section I will present results from a one proposed fabrication method. Figure 23 shows the initial fabrication plan, but I will explain how certain results found during the plasma etch step made me deviate from this plan.

First, a rectangular glass microscope slide (75 mm x 26 mm) was cleaved into three roughly square chips (~25 mm x 26 mm). This was performed outside of a cleanroom, so an acetone and IPA rinse was performed before entering the cleanroom. The glass slide was then cleaned in Piranha solution for ten minutes. These glass slides are considered “dirty” glass, since the content of them is less than 99% SiO_2. Because of this lack of purity these chips could not be etched in the ICP-Fluorine. To circumvent this, a thick 5 μm layer of PECVD SiO_2 was deposited on the chips. This cover layer of SiO_2 can be etched without contaminating the etch chamber.

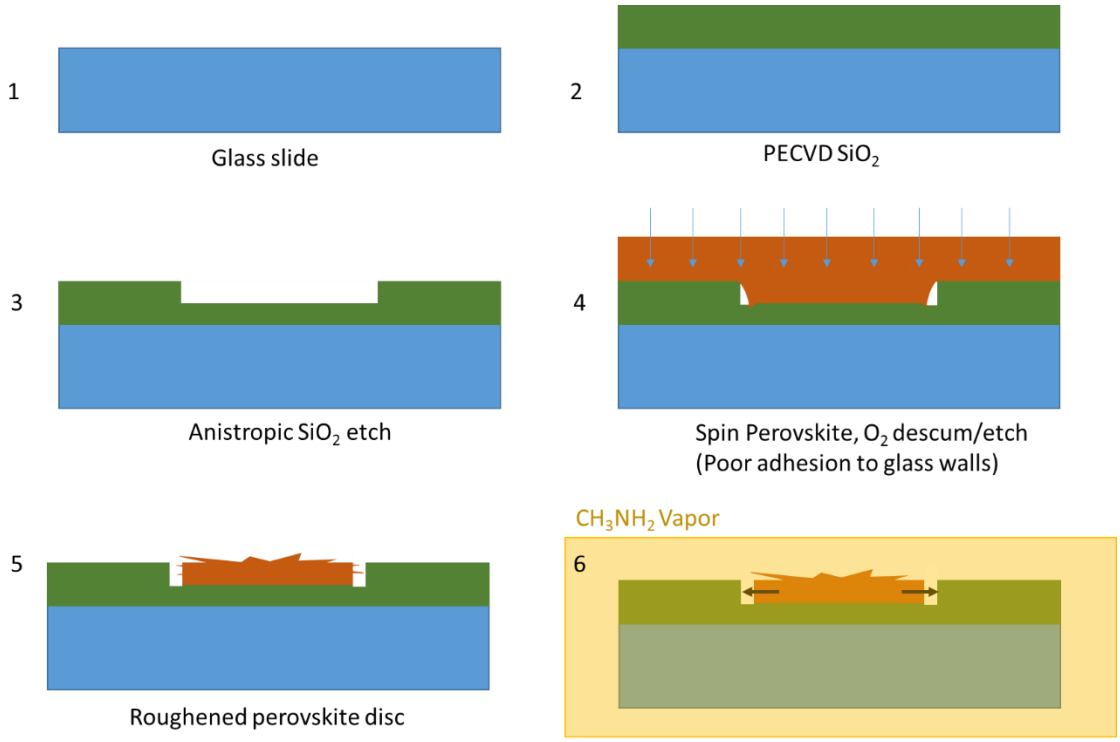

Figure 23: Fabrication process for creating perovskite microdiscs embedded in glass.

The chips were then patterned with photolithography. First, multiple patterns were written on the photomask, allowing us to write a variety of hole diameters: 5, 10, 20, or 40 μm. The circles are arranged in a rectangular lattice, with each circle being separated from its neighbor by 1 mm. This rather large separation distance was chosen in the hopes that the spinning of perovskite over this patterned glass is not significantly different than spinning on non-patterned glass. Whether this precaution is necessary remains unclear.

A ~1.2 μm layer of AZ1512 photoresist was spin-coated onto the glass substrates. I suggest treating the glass slides with HMDS before spinning photoresist in order to increase resist adhesion. In this particular process, no HMDS treatment was performed and only one out of seven chips had adequate resist adhesion for further processing. This became evident after developing the chips. For the chips with poor resist adhesion, I could see bubble-like patterns

where the holes should be. This was most likely due to water being trapped under the photoresist layer that was peeling away from the substrate around the developed features.

Etching was performed in the Oxford ICP-Fluorine. After the glass was etched, the remaining photoresist was stripped using an O_2 clean recipe. The resulting features were measured via stylus profilometry to be ~250 nm.

The chips were then given to Zhibin Yang in Professor Alex Jen's research group. A 500 nm layer of perovskite was spin-coated onto the chip. 500 nm is the thickest layer that can be controllably spin-coated onto the substrate, and this thickness was chosen in the hopes that the spin would be approximately planar, as opposed to conforming to the pattern geometry. Unfortunately, the spin was conformal according to stylus profilometry measurements. It is possible that the perovskite layer could be made planar by performing a MA vapor treatment to the film.

Assuming the perovskite layer is planar, the next step is to etch the perovskite layer until perovskite remains only in the patterned holes. An O_2 descum recipe was used on unpatterned test chips, and a yellow residue was left behind that could not be removed by the O_2 recipe. An Ar recipe was also attempted, which due to the inertness of Ar should be a purely physical etch. This etch left behind a powdery black residue. It seems reasonable that Pb is difficult to physically sputter, which may cause a residue to be left behind. Because of the unclear results of these etches, I never attempted an etch of the patterned chip.

In the hopes that we may still see some resonance from the glass chip despite it having an excessive amount of perovskite above the patterned features, an MA vapor treatment was performed and the PL was measured. The vapor treatment was necessary in this case, since it is highly unlikely that the perovskite layer conformed to the patterned glass walls during the spin-

coating step. The MA vapor treatment would hopefully solve this problem by liquefying and recrystallizing the perovskite on the glass walls. The patterned structures were pumped using a 405 nm laser, and the PL was measured both on and off the patterned structures. These plots are shown in Figure 24.

The measured PL curves raise several questions. First of all, it appears that there is some resonance occurring in the structures, since there are consistently spaced peaks that seem to indicate the different modes of resonance. Furthermore, the wavelength separation of these peaks (i.e. the free spectral range) is approximately 3 nm, which is what one would expect from the whispering-gallery modes supported by a 20 μm disc with an index of ~2.7. However, when the PL is measured on an unpatterned portion of the chip the same peaks can still be seen, which seems to suggest that these features of the spectrum are not arising due to the disc structures. It is likely that these small resonances are Fabry-Perot modes supported by the PECVD SiO_2 layer that was deposited on the glass slides.

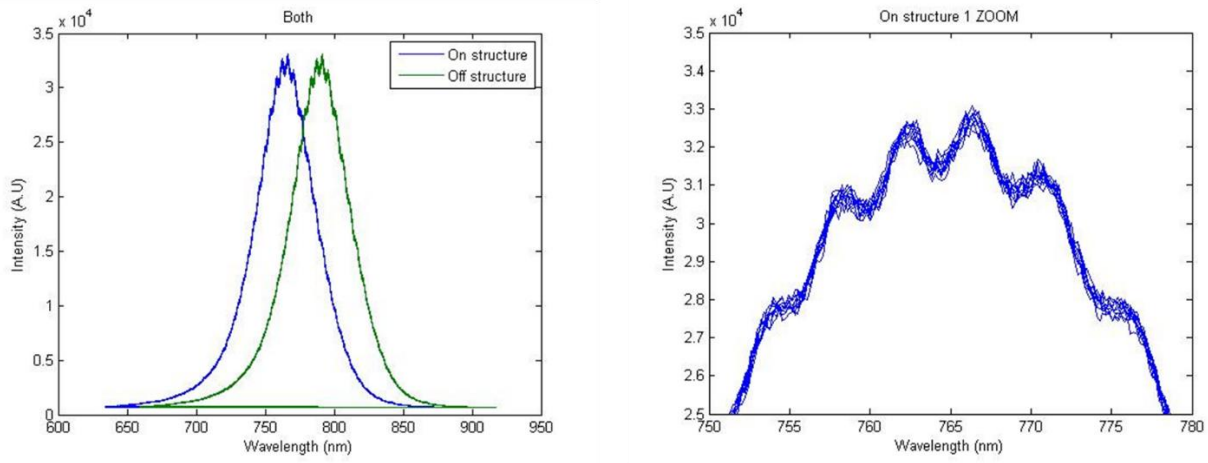

Figure 24: PL measurements taken on and off the microdisc structures.

Another unclear detail of these results is the ~3% blue shift in the PL measurement spectrum when measured on the structure compared to off the structure. A ~7% blue-shift is to

be expected from perovskite treated in MA vapor [4]. However, it seems unlikely that the location at which the off-structure PL measurement was taken was completely untreated by the MA vapor. This may indicate an issue with the way I performed the MA vapor treatment.

4.3 Suggested Future Work

Unless one can devise a method of smoothening patterned perovskite structures without significantly altering their patterned structure, I do not believe direct patterning using EBL is a feasible approach. EBL is an expensive process that was utilized purely based on the solvents used in a standard EBL process. Even though EBL offers some of the best resolution in lithography, this resolution is completely lost when the pattern is transferred to the perovskite. If these problems can be solved, the advantage would be that practically any devisable perovskite structure could be patterned via conventional methods.

If this direction is to be pursued, I suggest first characterizing the RIE etch of perovskite. A potential solution for this may be to combine O_2 and Ar in the etch chemistry. An O_2 etch is primarily governed by a chemical reaction between the oxygen plasma and the substrate surface. This O_2 etch left behind a yellow residue which may be undesirable for many applications. However, a subsequent Ar etch is capable of removing this residue. I suggest looking into etching with both O_2 and Ar, either simultaneously or sequentially.

I hypothesize that a high-quality resonant structure can be made from chemically reflowing perovskite on a pre-existing patterned structure without the need to etch the perovskite, and that this is a promising direction for this research. Unfortunately, the fabrication method in the previous section was flawed in numerous ways. I had assumed the RIE etch was a viable approach, and did not anticipate any issues with residue being left behind. It is possible that the

need for an RIE etch could be avoided by instead spin-coating a very thin layer of perovskite, which may conform to the patterned structures during the reflow process.

Another issue is the fabrication of the glass slides is not yet well characterized. It is highly likely that the patterned glass features were roughened by the etch. Since the perovskite-glass interface serves as the boundary for the perovskite disc, a roughened glass wall may preclude the structure from resonating. The method I suggest to investigate first would be using hydrogen silsesquioxane (HSQ). HSQ is a negative resist that can be patterned with EBL. It is not a polymer resist, but rather spin-on glass that can be as thick as 250 nm according to WNF staff.

Chapter 5. Electrically-Pumped Distributed Feedback Perovskite Laser

In this chapter I propose a perovskite DFB laser structure capable of being electrically pumped. DFB semiconductor lasers have proven to be well-suited for industrial applications, with one of their most desirable features being a tunable single-frequency output. There does not yet exist any electrically-pumped solution-processed semiconductor laser, but perovskite's extraordinary properties make it a strong candidate for filling this role [2].

DFB lasers operate on the same principles as a PhC, so the background information in Section 2.2.1 is applicable. Positive optical feedback is provided via Bragg scattering from a periodic structure, which is described by Equation 2.20. The critical components of a basic DFB laser are 1) a waveguide element that keeps the lasing mode confined laterally, 2) a corrugated structure, such as a grating, that provides optical feedback along the entire gain region (hence the term "distributed feedback"). The wavelengths at the two edges of the grating's stop-band resonate within the grating. Of these two resonant wavelengths, the wavelength that will experience more optical gain is difficult to predict, and is sensitive to the coupling strength of the grating and the lasing mode, as well as the spontaneous emission spectrum of the gain medium [44]. In practice, defects in the structure can cause one wavelength to be favored over the other. These defects can be introduced deliberately, as is the case for a $\lambda/4$ phase-shifting defect, or unintentionally by material and fabrication defects [45].

Saliba *et al.* demonstrated a structured perovskite device that exhibits DFB resonance, but it is unclear whether optically-pumped lasing was achieved [14]. Perovskite is conformally evaporated onto a nanoimprinted second-order grating structure and optically pumped. While DFB resonance was measured, the Q-factor of this resonance must have been adversely affected by the lack of a waveguide element, and thus the lack of lateral confinement of the DFB mode.

Furthermore, the nanoimprinted resist that formed the corrugated grating structure is not a suitable material for electrical pumping.

Figure 25 shows a proposed structure that features both a waveguide element and materials that permit electrical excitation. The structure is nearly identical to existing perovskite solar cell structures [46], except for the addition of patterned features that constitute the waveguide and grating required for a DFB laser. The bottom electrode is indium tin oxide (ITO), which functions as a transparent electrode. To form the waveguide, a strip of ITO is etched and filled in with NiO. NiO is a p-type semiconductor that functions as a hole transporting layer (HTL). A PEDOT:PSS layer lies above the ITO/NiO, and functions as another HTL. Since PEDOT:PSS is a soft material, it is capable of being directly patterned by nanoimprint lithography (NIL) [47]–[49]. Perovskite is then spin-coated over the PEDOT:PSS layer, followed by the deposition of an n-type electron transport layer (ETL) and finally the deposition of a top electrode. The ETL may have to be thick (>500 nm) so that the top electrode does not absorb the optical energy of the DFB mode [2]. This structure forms a PIN diode capable of being electrically pumped via a forward-bias current.

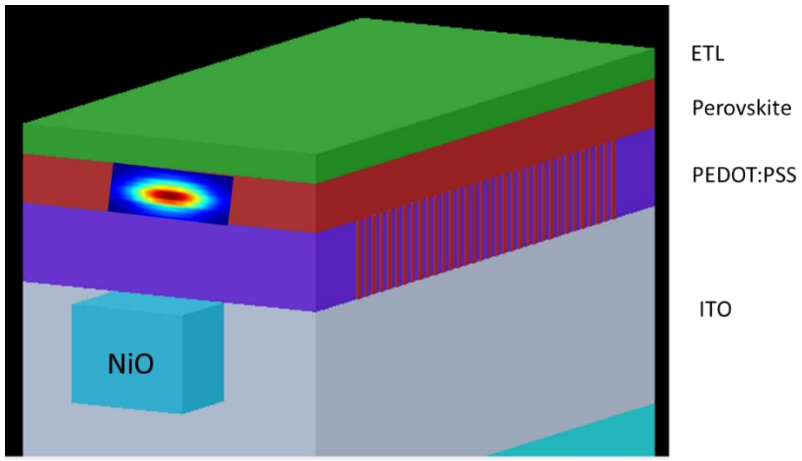

Figure 25: The proposed DFB laser structure. The top electrode is not pictured.

The index of refraction of each material is critical to the performance of this device, so the approximate indices of ITO, NiO, PEDOT:PSS, and $CH_3NH_3PbI_3$ perovskite are summarized in Table 1. Since perovskite has the largest index of all of these materials, the lasing mode will desirably be confined to the perovskite layer. The lasing mode will feature evanescent tails that penetrate into the surrounding layers, so the index of refraction of each layer affects the confinement of the mode. This enables us to confine the mode laterally by replacing a strip of low-index ITO with high-index NiO. Intuitively, this creates a region of high effective index, surrounded on both sides by a region of low effective index, which is shown in Figure 26.

Table 1: Refractive indices of DFB laser materials

Material	Refractive index
ITO	1.95 [50]
NiO	2.2 [51]
PEDOT:PSS	1.5 [50]
Perovskite	~2.5 [50]

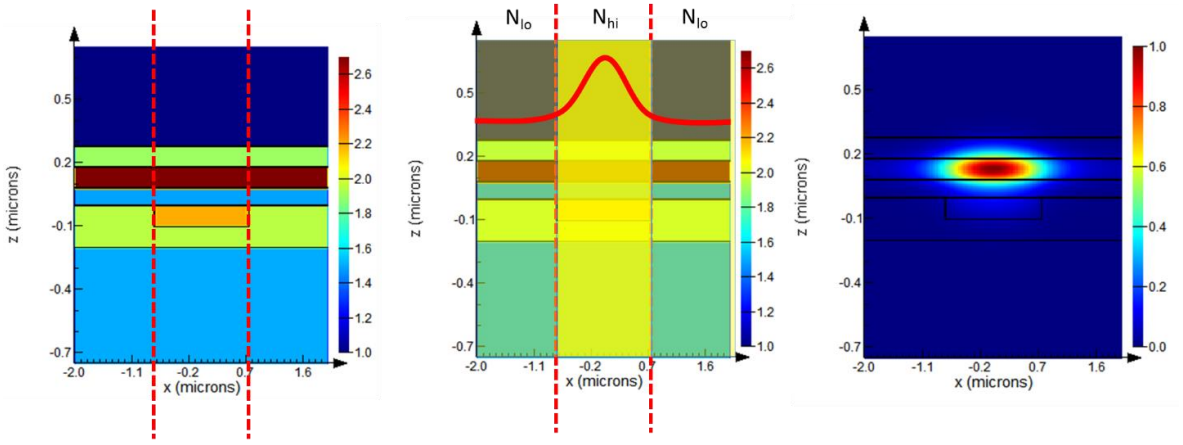

Figure 26: (Left) A cross-sectional view of the DFB laser structure waveguide. (Center) The effective indices of the various regions of the DFB. The solid red line indicates the magnitude of the electric field. (Right) The simulated waveguide mode confined in the perovskite layer.

The fabrication plan for this device is a combination of steps that have already been reported in literature. First, ITO is sputtered on a glass slide. ITO on glass is an inexpensive commercial product. Photoresist is then spin-coated onto the ITO and the waveguide strip is written via standard photolithography. Next, the ITO is partially etched via ICP-RIE using a $Cl_2/BCl_3/Ar$ recipe. This ITO etch recipe was developed by Joo *et al.*, resulting in the smooth ITO shown in Figure 27 [52]. At this point, the photoresist should not be stripped away. Instead, NiO is directionally evaporated such that the trenches that were just etched in the ITO are filled. Now the photoresist can be stripped, which lifts off the NiO on the photoresist. The only NiO remaining will be placed precisely in the trenches of the ITO layer. Next, PEDOT:PSS is spin-coated onto the chip and patterned via NIL, using a patterned silicon chip as a stamp. Finally, the perovskite, ETL, and top electrode are deposited using any of the established methods that already exist in perovskite solar cell structures.

Ideally, the amount of NiO deposited should be as close as possible to the amount of ITO that was etched. This can be done in the following manner. When etching the ITO, etch two chips simultaneously. Strip the photoresist on one of the chips, and measure the amount of ITO that was etched using profilometry. Using an evaporator with a crystal quartz monitor, deposit the same amount of NiO onto the other ITO chip, and proceed with the fabrication.

Another advantage of this fabrication technique is its scalability. The nanoimprinted features can be scaled simply by using a different silicon stamp. While NIL of PEDOT:PSS cannot achieve high aspect ratios, this is not an issue for DFB lasers since the corrugations of the grating are generally shallow. Thus, scaling of the grating element is primarily limited by the minimum writable feature size on silicon. The fabrication of the NiO strip is not altered by

changing its length or width over a reasonable range for waveguide dimensions. This design scalability is a particularly beneficial trait, since the emission wavelength of perovskite is highly tunable. The proposed structure could therefore accommodate practically any solution-processed perovskite.

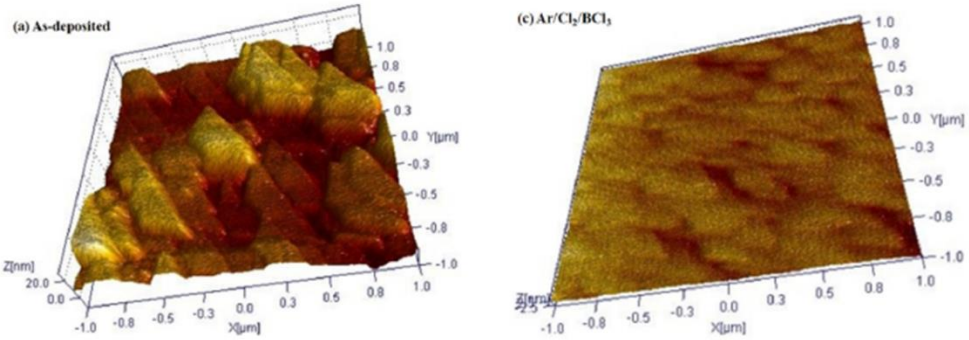

Figure 27: AFM images of (left) and as-deposited ITO layer and (right) an ITO layer etched in an $Ar/Cl_2/BCl_3$ plasma. [52]

Simulation of this device can be done using both Lumerical FDTD and using MATLAB scripts available from the textbook *Distributed feedback semiconductor lasers* by John Carroll, James Whiteaway, and Dick Plumb [44]. DFB lasers are large compared to the structures simulated in Chapters 3 and 4, so simulating the resonance in a full 3D numerical simulation is too computationally taxing and time consuming. However, Lumerical FDTD can construct the modal profile of a 2D cross section of the structure and estimate the effective index of the mode. This result can then be applied to the MATLAB scripts, which use a faster, theoretical approach to simulate lasing. The simulated lasing spectrum, as well as specific parameters for a feasible perovskite DFB structure, are shown in Figure 28.

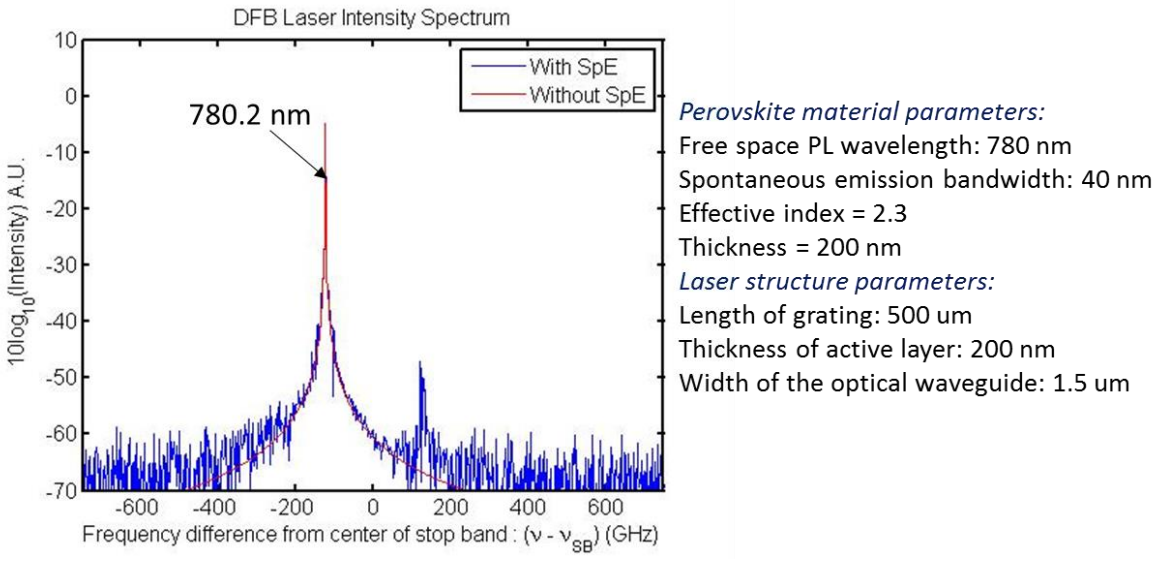

Figure 28: The simulated intensity spectrum of the proposed perovskite DFB laser. The random fluctuations are included to simulate spontaneous emission.

Chapter 6. Conclusions and Future Directions

This thesis presents the research performed in designing and fabricating a perovskite micro-cavity laser. The favorable light absorption and light emission properties of $CH_3NH_3PbI_3$ perovskites makes it a leading candidate as a new laser gain medium material. The main issue in realizing high-quality perovskite lasers is its inability to be patterned by most conventional fabrication techniques such as standard photolithography. EBL shows some promise, as various chemicals used in EBL seem to be compatible with perovskite. However, any nano-scale pattern defined by EBL cannot easily be transferred to perovskite by a dry etching recipe.

There are several directions that can be taken to couple perovskite to a high-quality cavity, or to form a high-quality cavity in perovskite itself. The work towards designing a high-Q PhC could be utilized and built upon to create a lasing cavity for perovskite. As long as one can devise a way to couple perovskite to the PhC without significantly altering its performance, such as by using the method suggested in Section 3.4, then a high-Q perovskite laser could potentially be fabricated.

Another direction is utilizing chemical reflow to create a smooth perovskite structure. If this reflow process is indeed capable of creating smooth perovskite structures as the literature suggests, then this opens up a huge amount of options for potential lasing structures. There is an additional benefit to this method. The research of perovskite light-emitters is predicated on the potential for perovskite solar cells to approach the SQ limit. Reaching this limit is an active frontier in solar cell research, and the efficiency and material properties of thin film perovskite is still improving. Since the reflow technique presented here is based on post-deposition methods that are on the forefront of photovoltaics research, the perovskite quality should be excellent.

The final method is to pattern a perovskite solar cell structure to create a DFB laser diode. The benefits of this structure include scalability that can accommodate the full range of perovskite emission wavelengths, and the ability to be electrically pumped. Solution-processed electrically-pumped lasers have not yet been realized, but perovskite could be the first to fill this role due to its extraordinary photonic properties.

References

[1] W. Shockley and H. J. Queisser, “Detailed Balance Limit of Efficiency of p-n Junction Solar Cells,” *J. Appl. Phys.*, vol. 32, no. 3, pp. 510–519, Mar. 1961.

[2] B. R. Sutherland and E. H. Sargent, “Perovskite photonic sources,” *Nat. Photonics*, vol. 10, no. 5, pp. 295–302, May 2016.

[3] Z. Zhou, Z. Wang, Y. Zhou, S. Pang, D. Wang, H. Xu, Z. Liu, N. P. Padture, and G. Cui, “Methylamine-Gas-Induced Defect-Healing Behavior of CH3NH3PbI3 Thin Films for Perovskite Solar Cells,” *Angew. Chem. Int. Ed.*, vol. 54, no. 33, pp. 9705–9709, Aug. 2015.

[4] T. Zhao, S. T. Williams, C.-C. Chueh, D. W. deQuilettes, P.-W. Liang, D. S. Ginger, and A. K.-Y. Jen, “Design rules for the broad application of fast (<1 s) methylamine vapor based, hybrid perovskite post deposition treatments,” *RSC Adv*, vol. 6, no. 33, pp. 27475–27484, 2016.

[5] S. D. Stranks, G. E. Eperon, G. Grancini, C. Menelaou, M. J. P. Alcocer, T. Leijtens, L. M. Herz, A. Petrozza, and H. J. Snaith, “Electron-Hole Diffusion Lengths Exceeding 1 Micrometer in an Organometal Trihalide Perovskite Absorber,” *Science*, vol. 342, no. 6156, pp. 341–344, Oct. 2013.

[6] S. Chen, K. Roh, J. Lee, W. K. Chong, Y. Lu, N. Mathews, T. C. Sum, and A. Nurmikko, “A Photonic Crystal Laser from Solution Based Organo-Lead Iodide Perovskite Thin Films,” *ACS Nano*, vol. 10, no. 4, pp. 3959–3967, Apr. 2016.

[7] Z.-K. Tan, R. S. Moghaddam, M. L. Lai, P. Docampo, R. Higler, F. Deschler, M. Price, A. Sadhanala, L. M. Pazos, D. Credgington, F. Hanusch, T. Bein, H. J. Snaith, and R. H. Friend, “Bright light-emitting diodes based on organometal halide perovskite,” *Nat. Nanotechnol.*, vol. 9, no. 9, pp. 687–692, Sep. 2014.

[8] F. Deschler, M. Price, S. Pathak, L. E. Klintberg, D.-D. Jarausch, R. Higler, S. Hüttner, T. Leijtens, S. D. Stranks, H. J. Snaith, M. Atatüre, R. T. Phillips, and R. H. Friend, “High Photoluminescence Efficiency and Optically Pumped Lasing in Solution-Processed Mixed Halide Perovskite Semiconductors,” *J. Phys. Chem. Lett.*, vol. 5, no. 8, pp. 1421–1426, Apr. 2014.

[9] H. Zhu, Y. Fu, F. Meng, X. Wu, Z. Gong, Q. Ding, M. V. Gustafsson, M. T. Trinh, S. Jin, and X.-Y. Zhu, “Lead halide perovskite nanowire lasers with low lasing thresholds and high quality factors,” *Nat. Mater.*, vol. 14, no. 6, pp. 636–642, Jun. 2015.

[10] J. Feng, X. Yan, Y. Zhang, X. Wang, Y. Wu, B. Su, H. Fu, and L. Jiang, “‘Liquid Knife’ to Fabricate Patterning Single-Crystalline Perovskite Microplates toward High-Performance Laser Arrays,” *Adv. Mater.*, vol. 28, no. 19, pp. 3732–3741, May 2016.

[11] G. Xing, N. Mathews, S. S. Lim, N. Yantara, X. Liu, D. Sabba, M. Grätzel, S. Mhaisalkar, and T. C. Sum, “Low-temperature solution-processed wavelength-tunable perovskites for lasing,” *Nat. Mater.*, vol. 13, no. 5, pp. 476–480, May 2014.

[12] S. D. Stranks and H. J. Snaith, “Metal-halide perovskites for photovoltaic and light-emitting devices,” *Nat. Nanotechnol.*, vol. 10, no. 5, pp. 391–402, May 2015.

[13] S. Chen, W. K. Chong, J. Lee, K. Roh, E. Sari, N. Mathews, T. C. Sum, and A. Nurmikko, “Optically Pumped Distributed Feedback Laser from Organo-Lead Iodide Perovskite Thin Films,” 2015, p. SM2F.6.

[14] M. Saliba, S. M. Wood, J. B. Patel, P. K. Nayak, J. Huang, J. A. Alexander-Webber, B. Wenger, S. D. Stranks, M. T. Hörantner, J. T.-W. Wang, R. J. Nicholas, L. M. Herz, M. B.

Johnston, S. M. Morris, H. J. Snaith, and M. K. Riede, “Structured Organic–Inorganic Perovskite toward a Distributed Feedback Laser,” *Adv. Mater.*, vol. 28, no. 5, pp. 923–929, Feb. 2016.
[15] Q. Zhang, S. T. Ha, X. Liu, T. C. Sum, and Q. Xiong, “Room-Temperature Near-Infrared High-Q Perovskite Whispering-Gallery Planar Nanolasers,” *Nano Lett.*, vol. 14, no. 10, pp. 5995–6001, Oct. 2014.
[16] T. J. Kippenberg, S. M. Spillane, and K. J. Vahala, “Demonstration of ultra-high-Q small mode volume toroid microcavities on a chip,” *Appl. Phys. Lett.*, vol. 85, no. 25, pp. 6113–6115, Dec. 2004.
[17] T. H. Maiman, “Stimulated Optical Radiation in Ruby,” *Nature*, vol. 187, no. 4736, pp. 493–494, Aug. 1960.
[18] A. E. Siegman, *Lasers*. Mill Valley, Calif: University Science Books, 1986.
[19] J. D. Joannopoulos, S. G. Johnson, J. N. Winn, and R. D. Meade, *Photonic Crystals: Molding the Flow of Light, Second Edition*, Second edition. Princeton: Princeton University Press, 2008.
[20] Q. Gong and X. Hu, Eds., *Photonic Crystals: Principles and Applications*, 1 edition. Pan Stanford, 2014.
[21] M. Skorobogatiy and J. Yang, *Fundamentals of Photonic Crystal Guiding*, 1 edition. Cambridge, UK ; New York: Cambridge University Press, 2009.
[22] S. John, “Strong localization of photons in certain disordered dielectric superlattices,” *Phys. Rev. Lett.*, vol. 58, no. 23, pp. 2486–2489, Jun. 1987.
[23] E. Yablonovitch, “Inhibited Spontaneous Emission in Solid-State Physics and Electronics,” *Phys. Rev. Lett.*, vol. 58, no. 20, pp. 2059–2062, May 1987.
[24] L. R. O. M. F.R.S, “CXII. The problem of the whispering gallery,” *Philos. Mag. Ser. 6*, vol. 20, no. 120, pp. 1001–1004, Dec. 1910.
[25] L. R. O. M. F.R.S, “IX. Further applications of Bessel’s functions of high order to the Whispering Gallery and allied problems,” *Philos. Mag. Ser. 6*, vol. 27, no. 157, pp. 100–109, Jan. 1914.
[26] C. V. Raman and G. A. Sutherland, “Whispering-Gallery Phenomena at St. Paul’s Cathedral,” *Nature*, vol. 108, no. 2706, p. 42, 1921.
[27] C. G. B. Garrett, W. Kaiser, and W. L. Bond, “Stimulated Emission into Optical Whispering Modes of Spheres,” *Phys. Rev.*, vol. 124, no. 6, pp. 1807–1809, Dec. 1961.
[28] S.-X. Qian, J. B. Snow, H.-M. Tzeng, and R. K. Chang, “Lasing Droplets: Highlighting the Liquid-Air Interface by Laser Emission,” *Science*, vol. 231, no. 4737, pp. 486–488, Jan. 1986.
[29] V. S. Ilchenko, A. A. Savchenkov, A. B. Matsko, and L. Maleki, “Nonlinear Optics and Crystalline Whispering Gallery Mode Cavities,” *Phys. Rev. Lett.*, vol. 92, no. 4, p. 43903, Jan. 2004.
[30] M. Gomilšek, “Whispering Gallery Modes,” *Univ. Ljubl. Ljubl. Semin.*, 2011.
[31] M. L. Gorodetsky, A. A. Savchenkov, and V. S. Ilchenko, “Ultimate Q of optical microsphere resonators,” *Opt. Lett.*, vol. 21, no. 7, p. 453, Apr. 1996.
[32] P. Jing, J. Wu, G. W. Liu, E. G. Keeler, S. H. Pun, and L. Y. Lin, “Photonic Crystal Optical Tweezers with High Efficiency for Live Biological Samples and Viability Characterization,” *Sci. Rep.*, vol. 6, Jan. 2016.

[33] S. Wu, S. Buckley, J. R. Schaibley, L. Feng, J. Yan, D. G. Mandrus, F. Hatami, W. Yao, J. Vučković, A. Majumdar, and X. Xu, "Monolayer semiconductor nanocavity lasers with ultralow thresholds," *Nature*, vol. 520, no. 7545, pp. 69–72, Apr. 2015.
[34] D. Van Thourhout and J. Roels, "Optomechanical device actuation through the optical gradient force," *Nat. Photonics*, vol. 4, no. 4, pp. 211–217, Apr. 2010.
[35] M. G. Scullion, A. Di Falco, and T. F. Krauss, "Slotted photonic crystal cavities with integrated microfluidics for biosensing applications," *Biosens. Bioelectron.*, vol. 27, no. 1, pp. 101–105, Sep. 2011.
[36] M. Eichenfield, J. Chan, R. M. Camacho, K. J. Vahala, and O. Painter, "Optomechanical crystals," *Nature*, vol. 462, no. 7269, pp. 78–82, Nov. 2009.
[37] Y. Lai, S. Pirotta, G. Urbinati, D. Gerace, M. Minkov, V. Savona, A. Badolato, and M. Galli, "Genetically designed L3 photonic crystal nanocavities with measured quality factor exceeding one million," *Appl. Phys. Lett.*, vol. 104, no. 24, p. 241101, Jun. 2014.
[38] S. Kita, K. Nozaki, and T. Baba, "Refractive index sensing utilizing a cw photonic crystal nanolaser and its array configuration," *Opt. Express*, vol. 16, no. 11, p. 8174, May 2008.
[39] J. E. Baker, R. Sriram, and B. L. Miller, "Two-dimensional photonic crystals for sensitive microscale chemical and biochemical sensing," *Lab. Chip*, vol. 15, no. 4, pp. 971–990, Feb. 2015.
[40] K. R. Williams, K. Gupta, and M. Wasilik, "Etch rates for micromachining processing-Part II," *J. Microelectromechanical Syst.*, vol. 12, no. 6, pp. 761–778, Dec. 2003.
[41] M. Liu, M. B. Johnston, and H. J. Snaith, "Efficient planar heterojunction perovskite solar cells by vapour deposition," *Nature*, vol. 501, no. 7467, pp. 395–398, Sep. 2013.
[42] O. Malinkiewicz, C. Roldán-Carmona, A. Soriano, E. Bandiello, L. Camacho, M. K. Nazeeruddin, and H. J. Bolink, "Metal-Oxide-Free Methylammonium Lead Iodide Perovskite-Based Solar Cells: the Influence of Organic Charge Transport Layers," *Adv. Energy Mater.*, vol. 4, no. 15, p. n/a-n/a, Oct. 2014.
[43] C. Wehrenfennig, M. Liu, H. J. Snaith, M. B. Johnston, and L. M. Herz, "Charge-carrier dynamics in vapour-deposited films of the organolead halide perovskite CH3NH3PbI3−xClx," *Energy Environ. Sci.*, vol. 7, no. 7, pp. 2269–2275, Jun. 2014.
[44] J. E. Carroll, J. Whiteaway, and D. Plumb, *Distributed Feedback Semiconductor Lasers*. IET, 1998.
[45] T. L. Koch and U. Koren, "Semiconductor lasers for coherent optical fiber communications," *J. Light. Technol.*, vol. 8, no. 3, pp. 274–293, Mar. 1990.
[46] J. W. Jung, C.-C. Chueh, and A. K.-Y. Jen, "A Low-Temperature, Solution-Processable, Cu-Doped Nickel Oxide Hole-Transporting Layer via the Combustion Method for High-Performance Thin-Film Perovskite Solar Cells," *Adv. Mater.*, vol. 27, no. 47, pp. 7874–7880, Dec. 2015.
[47] Y. Yang, K. Lee, K. Mielczarek, W. Hu, and A. Zakhidov, "Nanoimprint of dehydrated PEDOT:PSS for organic photovoltaics," *Nanotechnology*, vol. 22, no. 48, p. 485301, Dec. 2011.
[48] H. Hlaing, X. Lu, C.-Y. Nam, and B. M. Ocko, "Water-Vapor-Assisted Nanoimprinting of PEDOT:PSS Thin Films," *Small*, vol. 8, no. 22, pp. 3443–3447, Nov. 2012.
[49] J.-H. Choi, H.-J. Choi, J.-H. Shin, H.-P. Kim, J. Jang, and H. Lee, "Enhancement of organic solar cell efficiency by patterning the PEDOT:PSS hole transport layer using nanoimprint lithography," *Org. Electron.*, vol. 14, no. 12, pp. 3180–3185, Dec. 2013.

[50] C.-W. Chen, S.-Y. Hsiao, C.-Y. Chen, H.-W. Kang, Z.-Y. Huang, and H.-W. Lin, “Optical properties of organometal halide perovskite thin films and general device structure design rules for perovskite single and tandem solar cells,” *J. Mater. Chem. A*, vol. 3, no. 17, pp. 9152–9159, Apr. 2015.
[51] A. Venter and J. R. Botha, “Optical and electrical properties of NiO for possible dielectric applications,” *South Afr. J. Sci.*, vol. 107, no. 1/2, Jan. 2011.
[52] Y.-H. Joo, J.-C. Woo, K.-R. Choi, H.-S. Kim, J.-H. Wi, and C.-I. Kim, “Dry Etching of ITO Thin Films by the Addition of Gases in Cl_2 /BCl_3 Inductivity Coupled Plasma,” *Trans. Electr. Electron. Mater.*, vol. 13, no. 3, pp. 157–161, Jun. 2012.